Journal of Rock Mechanics and Geotechnical Engineering 18 (2026) 3703–3721

Contents lists available at ScienceDirect

Journal of Rock Mechanics and Geotechnical Engineering

journal homepage: www.jrmge.cn

Full Length Article

Diffusion of polymer permeation grouting in water-rich sand layers: Mathematical model and experimental validation

Jiasen Liang [a,b], Xueming Du [a,b,*], Lei Wang [a,b], Hongyuan Fang [a,b], Xiaohua Zhao [a,b], Bin Li [a,b], Kejie Zhai [a,b], Shanyong Wang [c]

[a] School of Water Conservancy and Transportation, Zhengzhou University, Zhengzhou, 450001, China
[b] Yellow River Laboratory (Hennan), Zhengzhou, 450001, China
[c] Priority Research Centre for Geotechnical Science and Engineering, School of Engineering, University of Newcastle, Callaghan, NSW, 2308, Australia

ARTICLE INFO

Article history:
Received 9 July 2025
Received in revised form
3 November 2025
Accepted 24 November 2025
Available online 7 January 2026

Keywords:
Water-rich sand layer
Model derivation
Permeation grouting
Polymer slurry
Diffusion mechanism

ABSTRACT

Water-rich sand layers are frequently encountered as adverse geological conditions during underground construction. Polymer slurry grouting has been widely recognized as an effective technique for reducing permeability and enhancing the stability of such strata. In this study, a mathematical model is established to describe the diffusion behavior of polymer slurry in porous media under dynamic water conditions and is further validated through laboratory experiments. The theoretical formulation of the slurry permeation process is developed based on Darcy's law, the Hagen–Poiseuille flow principle, and the physicochemical characteristics of the slurry. The derivation primarily focuses on analyzing the dynamic response of the slurry under the influence of water flow, considering the effects of flow velocity, grouting pressure, and sand-layer porosity on diffusion behavior. To verify the proposed model, a visualized grouting simulation system was designed to observe the diffusion process of polymer slurry in water-rich sand layers. The results demonstrate that slurry diffusion is significantly affected by grouting pressure, porosity, and water flow velocity. The observed staged diffusion characteristics, dynamic evolution patterns, and directional effects are in good agreement with theoretical predictions. Furthermore, the average relative deviations between the theoretical and experimental results for diffusion pressure and diffusion distance are both less than 25 %, confirming the reliability of the proposed model. Additionally, this study identifies distinct differences in slurry diffusion between porous and void media. In porous media, slurry propagation encounters greater hydraulic resistance, leading to rapid pressure attenuation and a limited diffusion range. Conversely, diffusion in void media occurs more smoothly due to the continuous cavity structure, resulting in slower pressure decay and a substantially larger diffusion radius. These findings elucidate the mechanisms governing slurry diffusion under dynamic water conditions and provide a theoretical basis for optimizing grouting parameters and improving construction efficiency in water-bearing strata.

1. Introduction

The hydrogeological environment encountered in underground engineering construction is highly complex. Adverse geological conditions, particularly water-rich sand layers, are frequently encountered in various infrastructure projects, including highways, railways, and tunnels (Xu et al., 2024; Du et al., 2025). Water-rich sand layers are characterized by high porosity, high water content, low cementation strength, poor self-stability, and high permeability (Long and Tan, 2020; Peng et al., 2024). During underground excavation, such layers are highly susceptible to geological hazards, including collapse, water inrush, sand boiling, and liquefaction, which may induce roadbed subsidence, railway interruption, pipeline blockage or fracture, and structural damage (Liu et al., 2025; Ma et al., 2025). These hazards pose serious threats to infrastructure safety and can result in substantial human

* Corresponding author. School of Water Conservancy and Transportation, Zhengzhou University, Zhengzhou, 450001, China.
E-mail address: 2007-dxm@163.com (X. Du).

Peer review under responsibility of Institute of Rock and Soil Mechanics, Chinese Academy of Sciences.

https://doi.org/10.1016/j.jrmge.2025.11.007

and economic losses. To mitigate these risks, grouting has been widely adopted as an effective technique for improving the mechanical properties of surrounding strata, enhancing stability, and reducing water inflow.

Under deep and high-stress conditions, the water-conducting channels within the strata may close, making the injection of traditional cement-based grouts difficult or even ineffective. In contrast, rapid-setting chemical grouts, particularly permeable polymer systems, exhibit superior adaptability to such environments (Liang et al., 2024, 2025). These grouts are characterized by short gelation times, typically ranging from several seconds to a few minutes. The application of fast-setting grouts can effectively control slurry diffusion distance and significantly enhance grouting efficiency (Budd and McKeown, 2010; Wang et al., 2022). Unlike conventional cement-based grouts, permeable polymer slurries require a static mixing system during onsite construction. In practice, the dual-component slurry flows through a static mixer installed at the injection port of the grouting pipe before being injected into the strata (Sharghi et al., 2017; Yang et al., 2024). This process leads to a viscosity that varies with both time and spatial position, thereby exhibiting pronounced spatiotemporal variability.

However, underground grouting engineering remains a "black-box" system owing to its highly concealed and complex nature (Cambefort, 1977; Letourneur, 1991). The theoretical development of polymer grouting has lagged far behind advances in grouting technologies, creating substantial challenges for both grouting design and the interpretation of slurry diffusion mechanisms (Zhang and Wang, 2024). The diffusion behavior of polymer slurry is governed by multiple interacting factors—including the intrinsic chemical reactions of the polymer, the dynamics of water flow, the adopted grouting method, and the pore structure of the injected medium—rendering the overall process inherently complex and difficult to predict or control. Consequently, practical engineering applications often proceed without sufficient theoretical guidance.

Several researchers have investigated the diffusion mechanisms of polymer slurries (Liang et al., 2022; Ke et al., 2024). Li et al. (2021) synthesized a novel polymer-based joint-filling material with excellent expansion characteristics, analyzed the influence of water quality on its swelling performance, and determined the optimal solid-to-liquid ratio of the slurry based on fluidity tests. Li et al. (2022) compared the fundamental physical properties of different polymers, including water-based polyurethane, oil-based polyurethane, and acrylates, and examined the grouting performance of chemically treated sand under varying polymer slurry-to-sand mass ratios (PS/S). Hao et al. (2023) established a visualized model of the polymer grouting process using the discrete element particle flow code (PFC2D) to overcome the limitations of conventional numerical methods in simulating the dynamics of polymer directional-splitting grouting.

Despite these advancements, existing theoretical models still exhibit significant limitations. Many studies neglect the coupling effects between chemical reaction kinetics and dynamic water flow, which are critical factors influencing slurry diffusion behavior under realistic hydrogeological conditions. For instance, traditional models often oversimplify the influence of water flow and fail to adequately capture the bidirectional feedback between flow velocity and chemical reaction rates during slurry diffusion. Moreover, most existing models disregard the dynamic characteristics of water flow in describing slurry diffusion within porous media, thereby constraining their predictive accuracy and applicability to dynamic water environments.

In porous media such as water-rich sand layers, slurry diffusion primarily occurs through permeation, and the pore structure plays a decisive role in controlling its behavior. Permeation grouting involves injecting slurry into granular soils to block water inflow and reinforce the strata without inducing structural damage. Ye et al. (2019) developed a hemispherical diffusion model for shield tunnel construction to determine the grouting pressure distribution and identify the effective diffusion radius. Zhu et al. (2023) employed computational fluid dynamics (CFD) and the discrete element method (DEM) to investigate the permeation and filtration behavior of cement-based grout in porous media. Sun et al. (2024) proposed an improved model that considers the time-dependent variations in pore fractal characteristics and slurry rheology. Wang et al. (2024) established a Bingham fluid-based diffusion model that integrates tortuosity, fractal theory, and viscosity evolution. Z. Li et al. (2022) analyzed slurry pressure attenuation and diffusion behavior using a two-phase seepage model, whereas Zhu et al. (2025) formulated a cylindrical–hemispherical diffusion model incorporating the time-dependent variation in slurry viscosity.

Several experimental studies have been carried out on permeation grouting to provide theoretical support and empirical validation for engineering practice. Markou et al. (2018) performed one-dimensional grouting experiments using ultrafine cement and established grouting suitability criteria based on their experimental results. Zhou et al. (2019) investigated the filtration behavior of slurry under constant-flow and constant-pressure conditions and reported that lower water-to-cement ratios increased the likelihood of slurry-induced clogging within seepage channels. Du et al. (2022) examined the diffusion characteristics of cement-based grouts in fractured rock and analyzed the influence of key parameters such as water-to-cement ratio, flow velocity, and particle mass fractal dimension.

In summary, the application of trenchless polymer grouting technology for treating adverse geological conditions is complicated by several interrelated factors, including the time-dependent variation in grout viscosity, the influence of dynamic water environments on grouting performance, the interaction between slurry and porous media, and the concealed nature of slurry diffusion during construction.

In this context, the present study develops a novel mathematical model to specifically address these challenges. The proposed model couples the chemical reaction kinetics of polymer slurry with the dynamics of water flow, explicitly considering the effects of flow velocity, grouting pressure, and sand-layer porosity on slurry diffusion. By incorporating Darcy's law, the Hagen–Poiseuille flow principle, and the physicochemical reaction characteristics of the slurry, the model provides a refined description of the dynamic polymer permeation grouting process in porous media. The derivation emphasizes the coupled effects of dynamic water flow and chemical reactions under realistic hydrogeological conditions, offering a more comprehensive understanding of slurry diffusion mechanisms. To verify the proposed model, a custom-designed visualized permeation grouting test system was employed to perform constant-pressure grouting experiments with permeable polymer slurry in water-rich sand layers. The experiments measured the spatiotemporal evolution and diffusion characteristics of the slurry, yielding empirical data that support the model predictions and demonstrate its applicability to engineering practice. Furthermore, a comparative analysis of real-time diffusion behavior between porous and void media was conducted, highlighting the robustness and versatility of the proposed model in simulating diverse grouting scenarios.

2. Fundamental assumptions for model derivation

The following assumptions are adopted in the development of the theoretical model:

(1) The diffusion of slurry within the porous medium (i.e. water-rich sand layer) is simplified as a one-dimensional flow along the grouting direction, designated as the *l*-axis. Lateral flow effects, such as radial or perpendicular diffusion, are neglected.
(2) The viscosity of the reacting mixture remains low until the system approaches the gel point, where it increases sharply toward infinity (Castro and Macosko, 1980; Baser and Khakhar, 1994). Assuming ideal mixing and rapid bubble nucleation, the polymer phase is treated as a continuous medium, and the slurry is approximated as a generalized Newtonian fluid (Seo and Youn, 2005).
(3) The seepage of slurry in the porous medium conforms to the generalized Darcy's law (Eq. (25)) (Dagan, 1979).
(4) The permeability (k) of the sand layer is assumed to depend on the porosity (φ) and the equivalent capillary radius (r_0), while the complex geometrical configuration of the pore structure is neglected.
(5) The slurry flow within individual pores or capillaries is assumed to obey the Hagen–Poiseuille law (Eqs. (8) and (9)), producing a parabolic velocity distribution with zero velocity at the pore wall (Wang and Xie, 2022).
(6) The viscosity of the slurry is assumed to increase exponentially due to the exothermic chemical reaction occurring during polymerization.
(7) The shear and velocity variations of the water flow are neglected. The background flow is considered steady, and its scouring effect is represented as a constant force acting on the slurry front.
(8) A constant-pressure grouting system is employed, with an adjustable pressure in the range of 0–6 MPa. For model derivation, the grouting pressure (p_0) is assumed to remain constant throughout the process.

3. Derivation of the dynamic water permeation grouting model

According to the energy conversion principle between hydrostatic and kinetic energy (Yuce and Muratoglu, 2015), when the direction of slurry diffusion is aligned with the water flow direction, the relationship can be expressed as

$$p_w = \frac{1}{2}\rho_w v^2 \tag{1}$$

Conversely, when the direction of slurry diffusion is opposite to that of the water flow, the relationship becomes

$$p_w = -\frac{1}{2}\rho_w v^2 \tag{2}$$

where ρ_w is the density of water (kg/m^3), v is the velocity of water flow (m/s).

As illustrated in Fig. 1, assuming that the static shear force exerted by the water on the slurry is negligible and the velocity variation is insignificant, the sum of forces along the radial centerline of a fluid microelement must be zero. The scouring force exerted by the water on the slurry is denoted as p_w. Based on this, the force balance in a cylindrical fluid microelement within a capillary tube is given by

$$\pi(\Delta r)^2 \Delta(p + p_w) - 2\pi\Delta r \Delta l \Delta\tau = 0 \tag{3}$$

where p is the grout pressure (Pa); Δr is the radial increment of the fluid microelement (m); Δl is the axial length of the fluid microelement along the diffusion direction (m); $\Delta\tau$ is the increment of shear stress acting on the lateral surface of the microelement (Pa).

Upon simplification:

$$\frac{\mathrm{d}(p + p_w)}{2\mathrm{d}l} = \frac{\mathrm{d}\tau}{\mathrm{d}r} \tag{4}$$

Integrating Eq. (4) with respect to the radial coordinate r, we obtain

$$\frac{\mathrm{d}(p + p_w)}{2\mathrm{d}l}(r + c_1) = \tau \tag{5}$$

where c_1 is the integration constant arising from integration with respect to the radial coordinate r. Subsequently, these integration constants c_i (i = 1, 2, 3, 4) are determined or eliminated through the application of appropriate boundary conditions.

According to Newton's law of viscosity:

$$\tau = \eta_{(t)}\frac{\mathrm{d}u_l}{\mathrm{d}r} \tag{6}$$

where $\eta_{(t)}$ is the time-dependent viscosity of the slurry; $\eta_{(t)} = Ae^{Bt} + C$, A, B, and C are empirical fitting parameters for viscosity; $\frac{\mathrm{d}u_l}{\mathrm{d}r}$ is the velocity gradient representing the rate of change of slurry velocity in the radial direction; and τ is the shear stress exerted on the slurry during flow.

Substituting Eq. (6) into Eq. (5) yields

$$\frac{\mathrm{d}(p + p_w)}{2\mathrm{d}l}(r + c_1) = \eta_{(t)}\frac{\mathrm{d}u_l}{\mathrm{d}r} \tag{7}$$

Applying the relevant boundary conditions $\left.\frac{\partial u_l}{\partial r}\right|_{r=0} = 0$ to Eq. (7), we derive

$$\frac{\mathrm{d}u_l}{\mathrm{d}r} = \frac{\mathrm{d}(p + p_w)}{2\eta_{(t)}\mathrm{d}l}r \tag{8}$$

Integrating Eq. (8) with respect to r, we obtain

$$u_l = \frac{\mathrm{d}(p + p_w)}{4\eta_{(t)}\mathrm{d}l}\left(r^2 + c_2\right) \tag{9}$$

where c_2 is the integration constant from the second integration of the velocity gradient with respect to r.

By applying the boundary conditions $u_l|_{r=r_0} = 0$ to Eq. (9), and subsequently substituting the results back, the final velocity distribution of the slurry in the radial direction is given by

$$u_l = \frac{\mathrm{d}(p + p_w)}{4\eta_{(t)}\mathrm{d}l}\left(r^2 - r_0^2\right) \tag{10}$$

For laminar flow in a cylindrical capillary, the average velocity of the slurry is obtained by integrating the velocity distribution over the entire cross-sectional area and then dividing by the area S. The expression for the average velocity is given by

$$\overline{u_l} = \frac{1}{S}\iint_S u_l(r)\mathrm{d}S \tag{11}$$

where S denotes the circular cross-sectional area with radius r_0, i.e. $S = \{r \mid \| r \| \le r_0\}$.

The integral is evaluated from the pipe center $r = 0$ to the pipe wall $r = r_0$, and the cross-sectional area of the circular pipe is πr_0^2. Substituting into the average velocity expression, we have

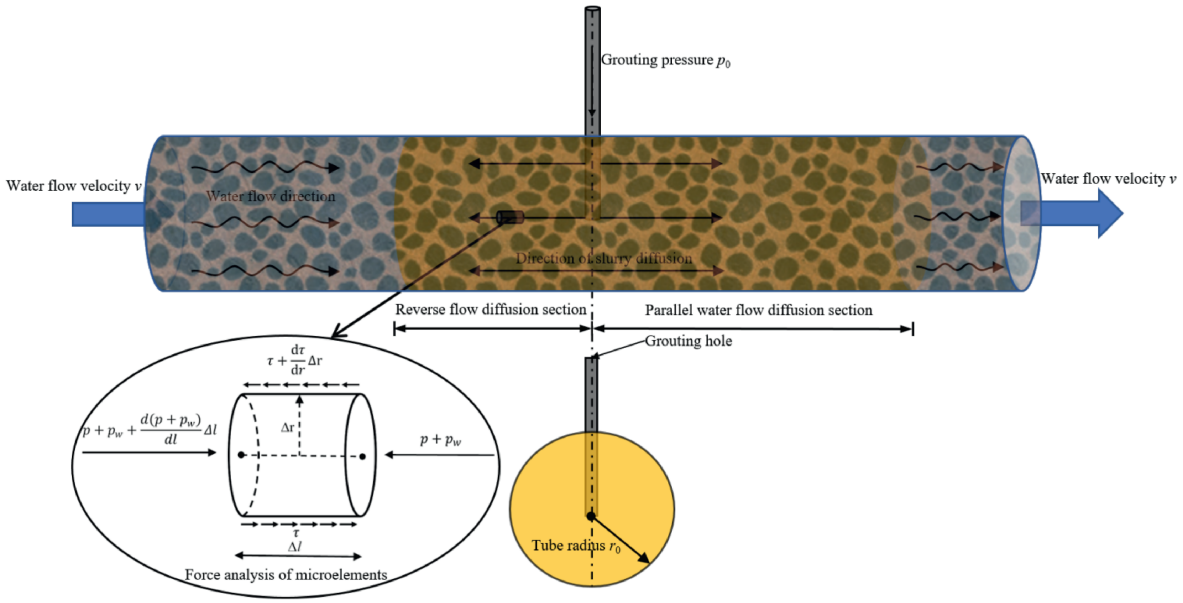

Fig. 1. Theoretical model of cylindrical slurry permeation and diffusion.

$$\overline{u_l} = \frac{1}{\pi r_0^2}\int_0^{r_0} u_l(r)\cdot 2\pi r dr \tag{12}$$

Solving the integral in Eq. (12), we obtain

$$\overline{u_l} = -\frac{r_0^2}{8\eta_{(t)}}\frac{\mathrm{d}(p+p_w)}{\mathrm{d}l} \tag{13}$$

In a void media, the unit flow rate q represents the volumetric flow passing through the pipe cross-section per unit time, expressed as

$$q = \pi r_0^2 \overline{u_l} \tag{14}$$

Rearranging Eq. (14) yields

$$\frac{\mathrm{d}(p+p_w)}{\mathrm{d}l} = -\frac{8q\eta_{(t)}}{\pi r_0^4} \tag{15}$$

Taking the indefinite integral of Eq. (15) with respect to l (the diffusion distance along the slurry injection direction), we get

$$p + p_w = -\frac{8q\eta_{(t)}}{\pi r_0^4} l + c_3 \tag{16}$$

where c_3 is the indefinite integration constant with respect to the diffusion distance l.

Applying the boundary condition at $l = l_m$, where $p + p_w = p_m$, gives

$$p + p_w = -\frac{8q\eta_{(t)}}{\pi r_0^4} l + p_m + \frac{8q\eta_{(t)}}{\pi r_0^4} l_m \tag{17}$$

Similarly, at $l = l_0$, where $p = p_0$, substituting into Eq. (17) yields

$$q = \frac{\pi r_0^4 (p_0 + p_w - p_m)}{8\eta_{(t)}(l_m - l_0)} \tag{18}$$

where p_0 is the injection (grouting) pressure (Pa); p_m is the hydrostatic pressure (Pa); l_m is the effective diffusion distance (m); l_0 is the radius of the grouting borehole (m); and r_0 is the radius of the idealized cylindrical pore or capillary (m).

Assuming that the injected slurry volume during a unit time period equals the volume required to increase the diffusion distance in that time, the following relationship holds

$$\int_0^{t_m} q\mathrm{d}t = \int_{l_0}^{l_m} \pi r_0^2 \mathrm{d}l \tag{19}$$

Substituting Eq. (18) into Eq. (19) and rearranging, we obtain

$$\frac{\pi r_0^4 (p_0 + p_w - p_m)}{8(l_m - l_0)}\int_0^{t_m} \frac{1}{\eta_{(t)}}\mathrm{d}t = \int_{l_0}^{l_m} \pi r_0^2 \mathrm{d}l \tag{20}$$

Through variable substitution and solving the definite integral $\int_0^{t_m} \frac{1}{\eta_{(t)}}\mathrm{d}t$ using special functions, the relationship between injection time t_m and diffusion distance l_m in a void medium can be expressed as

$$\frac{1}{BC}\ln\left[\frac{e^{Bt_m}(A+C)}{Ae^{Bt_m}+C}\right] = \frac{8(l_m - l_0)^2}{r_0^2(p_0 + p_w - p_m)} \tag{21}$$

By substituting Eq. (18) into Eq. (17), the pressure distribution of the grout within a cylindrical void medium can be expressed as

$$p + p_w = p_m + \frac{(p_0 + p_w - p_m)}{(l_m - l_0)}(l_m - l) \tag{22}$$

Substituting Eq. (18) into Eq. (15), the pressure gradient in the void medium becomes

$$\frac{\mathrm{d}(p+p_w)}{\mathrm{d}l} = -\frac{(p_0 + p_w - p_m)}{(l_m - l_0)} \tag{23}$$

Inserting Eq. (23) into Eq. (10), the average velocity distribution of the grout in the cylindrical void medium is obtained as

$$\overline{u_l} = \frac{r_0^2}{8(Ae^{Bt} + C)}\frac{(p_0 + p_w - p_m)}{(l_m - l_0)} \tag{24}$$

Eq. (24) describes the average velocity of laminar flow of chemically reactive grout in a cylindrical void, accounting for the time-dependent viscosity. In the case of one-dimensional seepage grouting in a porous medium, assuming identical force conditions

on the fluid element, the actual fluid velocity is denoted as v, and the seepage velocity is

$$V = \varphi\overline{u_l} = -\frac{\varphi r_0^2}{8\eta_{(t)}}\frac{\mathrm{d}(p+p_w)}{\mathrm{d}l} \tag{25}$$

According to Darcy's law, the seepage velocity is defined as

$$V = -\frac{k}{\eta_{(t)}}\frac{\mathrm{d}(p+p_w)}{\mathrm{d}l} \tag{26}$$

where k is the permeability coefficient, and $\frac{\mathrm{d}(p+p_w)}{\mathrm{d}l}$ is the pressure gradient. Eq. (25) conforms to the generalized form of Darcy's law.

By equating Eqs. (25) and (26), the permeability in one-dimensional seepage is expressed as

$$k = \frac{\varphi r_0^2}{8} \tag{27}$$

In porous media, the unit flow rate q represents the total volumetric flow rate through the pipe cross-section. Based on Darcy's law and porosity, the flow rate is given by

$$q = \varphi\pi r_0^2 u_{\mathrm{pore}} \tag{28}$$

Since fluid flows only through pore spaces rather than the entire cross-sectional area, the actual average velocity within the pores u_{pore} is expressed as

$$u_{\mathrm{pore}} = \frac{V}{\varphi} \tag{29}$$

Substituting Eq. (29) into (28) yields

$$q = -\frac{\pi r_0^2 k}{\eta_{(t)}}\frac{\mathrm{d}(p+p_w)}{\mathrm{d}l} \tag{30}$$

Rearranging Eq. (30), we obtain

$$\frac{\mathrm{d}(p+p_w)}{\mathrm{d}l} = -\frac{q\eta_{(t)}}{\pi r_0^2 k} \tag{31}$$

Integrating Eq. (31) with respect to l gives

$$p + p_w = -\frac{q\eta_{(t)}}{\pi r_0^2 k}l + c_4 \tag{32}$$

where c_4 is the indefinite integration constant with respect to the diffusion distance l (in the case of a porous medium).

Applying the boundary condition at $l = l_m$, where $p + p_w = p_m$, yields

$$p + p_w = p_m + \frac{q\eta_{(t)}}{\pi r_0^2 k}(l_m - l) \tag{33}$$

Applying the boundary condition at $l = l_0$, where $p = p_0$, the flow rate is derived as

$$q = \frac{\pi r_0^2 k(p_0 + p_w - p_m)}{\eta_{(t)}(l_m - l_0)} \tag{34}$$

Substituting Eq. (34) into Eq. (33) yields

$$p + p_w = p_m + \frac{(p_0 + p_w - p_m)}{(l_m - l_0)}(l_m - l) \tag{35}$$

Assuming the grout volume injected during a unit time interval equals the volume required to achieve the corresponding increase in diffusion distance, we have

$$\int_0^{t_m} q\mathrm{d}t = \int_{l_0}^{l_m} \pi r_0^2 \mathrm{d}l \tag{36}$$

By substituting Eqs. (27) and (34) into Eq. (36), and simplifying, the relationship between grouting time t_m and diffusion distance l_m in a porous medium is derived as

$$\frac{1}{BC}\ln\left[\frac{\mathrm{e}^{Bt_m}(A+C)}{A\mathrm{e}^{Bt_m}+C}\right] = \frac{8(l_m - l_0)^2}{\varphi r_0^2(p_0 + p_w - p_m)} \tag{37}$$

Finally, substituting Eqs. (31) and (34) into Eq. (26), the average velocity distribution of the grout within a cylindrical pipe in porous media is

$$V = \frac{k}{A\mathrm{e}^{Bt} + C}\frac{(p_0 + p_w - p_m)}{(l_m - l_0)} \tag{38}$$

4. Experimental validation of the theoretical model

A self-developed visualized seepage grouting simulation system was employed to perform a series of constant-pressure grouting experiments under flowing-water conditions. The experiments were designed to investigate the effects of key grouting parameters—namely, grouting pressure (p_0), porosity (φ), and water flow velocity (v)—on the diffusion characteristics of permeable polymer slurry. The objective was to examine the spatial and temporal evolution of slurry diffusion within a water-rich sandy stratum and to validate the proposed theoretical seepage grouting model for dynamic water conditions by comparing the experimental observations with theoretical predictions under different parameter scenarios.

4.1. Experimental materials

The grouting material used in the experiments was a permeable polymer supplied by Wanhua Energy-Saving Technology Co., Ltd. (Yantai, China). The polymer consists of two main components: a polyol-based solution (Component A) and an isocyanate-based solution (Component B). As illustrated in the schematic diagram, Component A contains hydrophilic low-viscosity polyether polyols, permeation diluents, surfactants, and catalysts, whereas Component B comprises isocyanates, permeation diluents, and flame retardants.

The primary chemical reaction mechanism of the permeable polymer involves the formation of urethane linkages through the reaction between the isocyanate groups in Component B and the hydroxyl groups in Component A. These urethane linkages constitute the hard segments of the polymer and contribute significantly to its cohesive energy. In addition, side reactions among isocyanate groups may produce isocyanate dimers or trimers, further enhancing the mechanical strength of the resultant polyurethane structure. The solidified polymer markedly improves the impermeability and mechanical integrity of the porous medium. Moreover, it exhibits outstanding durability, with strength that remains stable—or even increases slightly—over time under continuous water exposure.

Grout viscosity reflects the internal resistance of the slurry to flow and serves as a key parameter for evaluating its injectability. The viscosity of permeable polymer grout strongly influences its flow behavior and is therefore critical for understanding the diffusion mechanism of the slurry. To investigate the time-dependent viscosity characteristics of the permeable polymer

grout, a series of rotational viscometry tests were performed. The experimental procedure for viscosity measurement is illustrated in Fig. 2. Component A of the polymer grout has a density of 1.12 g/cm^3, whereas Component B has a density of 1.19 g/cm^3. Viscosity was measured using an SNB-2 rotational viscometer, which has a measurement range of 0.1–2 × 10^7 mPa s. Before mixing, both components were preheated in a water bath to a uniform temperature of 40 °C.

After the viscometer was mounted, a temperature probe was installed and connected to the instrument, which was then linked to a computer via Ethernet for real-time monitoring of viscosity variation. Owing to the rapid polymerization rate of the system, Rotor No. 1 was selected with a rotation speed of 6 r/min, appropriate for the expected viscosity range of 0–999.8 mPa s. The rotor type and speed were configured through the instrument interface, and the device was set to automatically record the viscosity over time. A rotor guard was installed to prevent potential mechanical damage during operation.

Upon completion of preheating, the two components were rapidly mixed and stirred five times using a glass rod. The temperature probe was fixed along the inner wall of the beaker, and measurements of grout viscosity and temperature were initiated immediately to capture the early-stage viscosity evolution and its variation with time.

As illustrated in Fig. 3, the time-dependent curves of viscosity and temperature for the permeable polymer grout exhibit a synchronous variation, confirming that the grout reaction is an exothermic process. During the initial stage (0–33 s), the viscosity of the polymer grout remains nearly constant, while the temperature increases slowly. In the subsequent stage (33–64 s), the viscosity begins to rise gradually, accompanied by an accelerated increase in temperature. Between 64 s and 84 s, both viscosity and temperature show a moderate acceleration in their rates of increase. In the final stage (84–100 s), a sharp rise in viscosity occurs simultaneously with a rapid temperature increase, indicating the onset of vigorous reaction and solidification of the polymer grout. The maximum temperature recorded during the process reaches 67.1 °C.

A curve-fitting analysis was conducted on the time-dependent viscosity data of the permeable polymer grout to characterize its rheological evolution. As illustrated in Fig. 3, the viscosity of the

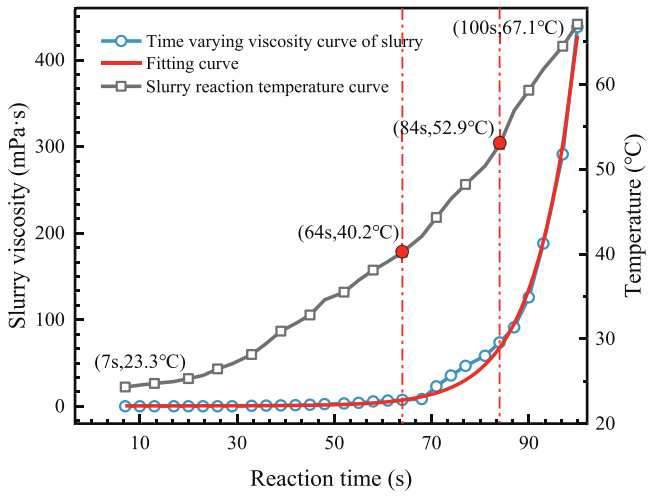

Fig. 3. Time-dependent curves of viscosity and temperature for the polymer grout.

grout exhibits an exponential increase with time. The optimal empirical fitting model can be expressed as follows:

$$\eta_{(t)} = Ae^{Bt} + C \tag{39}$$

where $\eta_{(t)}$ is the viscosity at time t (mPa s), and A, B, and C are empirical constants determined from the experimental data. The obtained values are $A = 8.82419$, $B = 0.38642$, and $C = 2.8782$. Physically, the constant C represents the initial viscosity of the polymer grout. The coefficient of determination for the fitting equation is $R^2 = 0.99$, indicating excellent agreement between the experimental and fitted data and confirming that the model accurately captures the viscosity evolution of the grout during the reaction process.

The sand used in the experiments was classified using the standard sieving method with a ZBSX-92A vibrating sieve shaker (see Fig. 4). The sieve apertures used were 4.75 mm, 2.36 mm, 1.18 mm, 0.6 mm, 0.3 mm, and 0.15 mm. Based on the sieving results, the sand samples were grouped into five particle-size ranges: 0.15–0.3 mm, 0.3–0.6 mm, 0.6–1.18 mm, 1.18–2.36 mm,

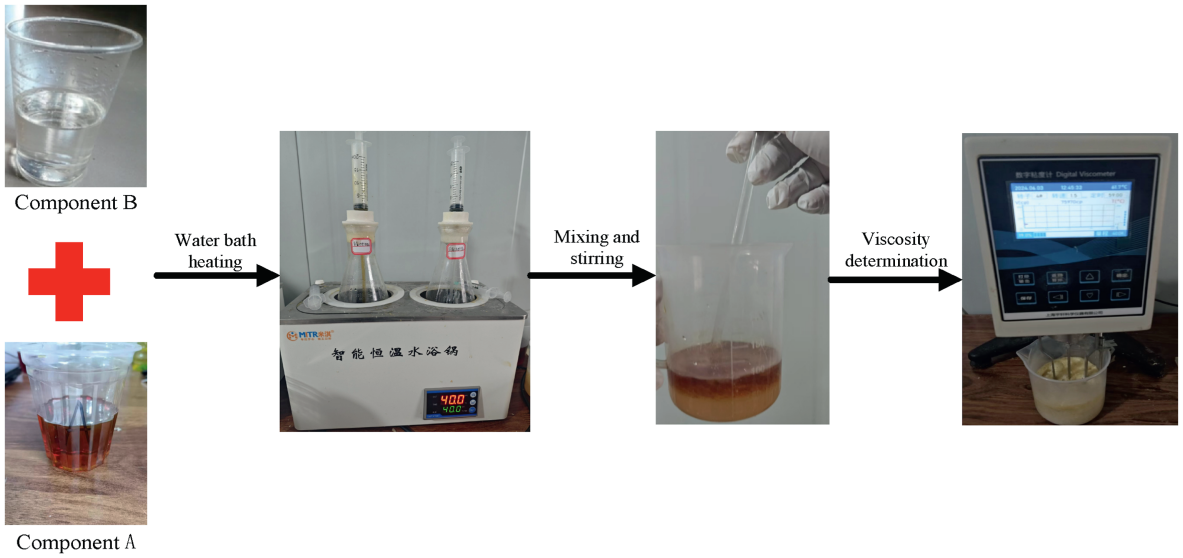

Fig. 2. Measurement of grout viscosity and temperature.

Fig. 4. ZBSX-92A vibrating sieve shaker.

Table 1
Particle size distribution of sand samples.

Sand Sample	Particle size distribution						Mean particle diameter(mm)
	0 mm < *particle size* < 0.15 mm	0.15 mm < *particle size* < 0.3 mm	0.3 mm < *particle size* < 0.6 mm	0.6 mm < *particle size* < 1.18 mm	1.18 mm < *particle size* < 2.36 mm	2.36 mm < *particle size* < 4.75 mm	
1	0.26 %	1.17 %	2.72 %	7.7 %	22.32 %	65.83 %	2.93
2	0.98 %	2.66 %	4.73 %	10.61 %	24.33 %	56.69 %	2.64
3	3.62 %	5.69 %	7.6 %	13.48 %	24.51 %	45.1 %	2.12

and 2.36–4.75 mm. The corresponding mean particle diameters for each group are listed in Table 1.

From the particle-size distribution curves, three gradation indices were calculated. The uniformity coefficient (C_u) characterizes the degree of particle-size uniformity, where $C_u > 5$ indicates poorly graded (non-uniform) sand. The coefficient of curvature (C_c) evaluates the continuity of the gradation curve, with values ranging between 1 and 3 representing well-graded sands. The detailed gradation parameters for the sand samples used in the tests are presented in Table 2. These indices are calculated as follows:

$$C_u = \frac{d_{60}}{d_{10}} \tag{40}$$

$$C_c = \frac{d_{30}^2}{d_{60} d_{10}} \tag{41}$$

where C_u is the coefficient of uniformity; C_c is the coefficient of curvature; d_{60} is the particle diameter corresponding to 60 % finer by mass (i.e., the diameter below which 60 % of the particle mass lies), also known as the characteristic diameter or confining diameter; d_{30} is the particle diameter corresponding to 30 % finer by mass (i.e., the diameter below which 30 % of the particle mass lies); and d_{10} is the particle diameter corresponding to 10 % finer by mass (i.e., the diameter below which 10 % of the particle mass lies), also known as the effective diameter.

Table 2
Gradation indices and porosity of sand samples.

Sand sample	Uniformity coefficient C_u	Coefficient of curvature C_c	Porosity (%)
1	3.173	1.334	30.7
2	4.435	1.385	37
3	8.767	1.705	42.4

4.2. Experimental system

The experimental setup employed in this study is comprised of four main components: a dual-component grouting system, a visualized slurry diffusion system, a dynamic water supply system, and a monitoring system, as illustrated in Fig. 5.

The dual-component grouting system used in this study primarily comprises an air compressor and a dual-component grouting machine (see Fig. 6). The grouting machine is equipped with diaphragm pumps (for slurry injection and material extraction from the storage tanks), separate storage tanks for Components A and B, a mechanical stirrer (to prevent material sedimentation), a grouting control panel (for setting injection parameters), a grouting gun, and a heating unit. This system enables both constant-pressure and constant-flow grouting operations for the reinforcement and remediation of weak geological formations. The grouting pressure can be adjusted within the range of 0–6 MPa. The heating unit allows the preheating of Components A and B in their respective storage tanks to temperatures between 25 °C and 55 °C.

The custom-designed visualized slurry diffusion system (Fig. 7) consists of a cylindrical acrylic chamber with a height of 150 cm and an inner diameter of 6 cm, along with pressure sensors and water control valves. The diffusion chamber is assembled from three cylindrical segments with heights of 40 cm, 70 cm, and 40 cm, respectively, which are connected by tie rods and bolts. Silicone gaskets are installed between adjacent acrylic segments to ensure leak-proof sealing and to facilitate rapid disassembly for material filling and sensor installation. Circular inlet and outlet openings (2 cm and 3 cm in diameter, respectively) are positioned at both ends of the device to allow unobstructed fluid flow.

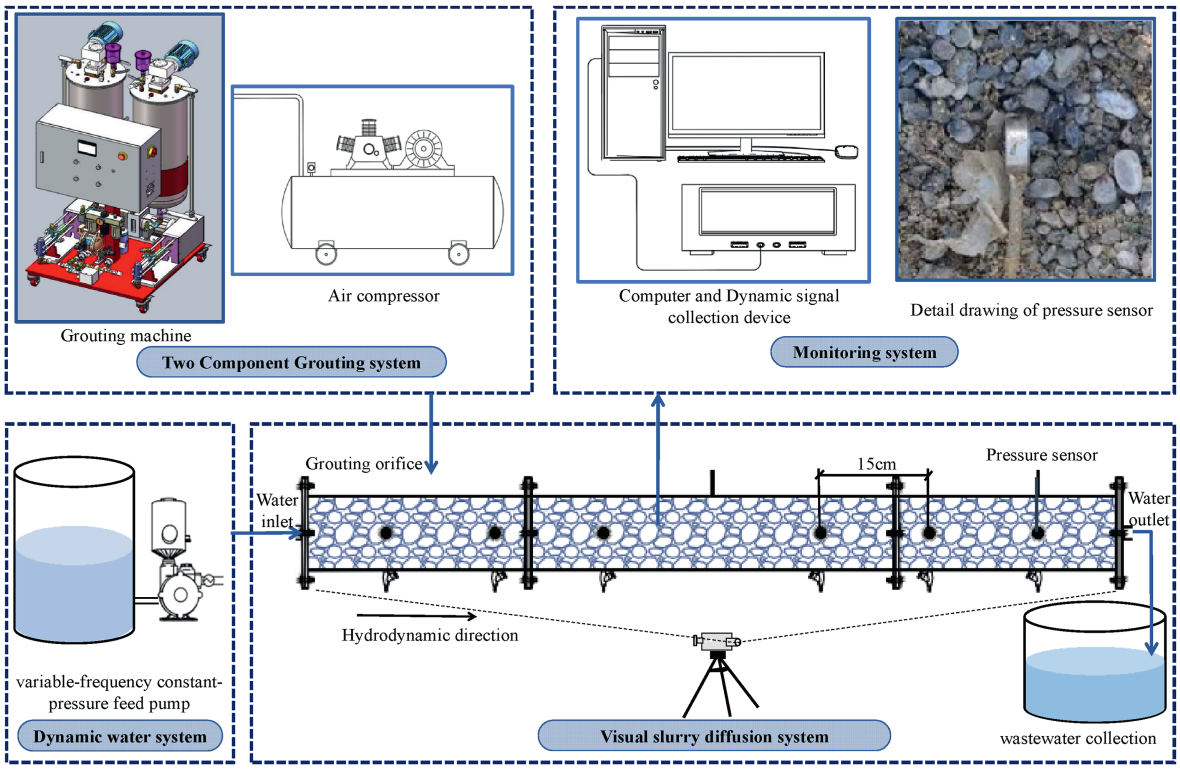

Fig. 5. Schematic diagram of the experimental setup.

Polypropylene random (PPR) pipes are used to connect the diffusion chamber to the dynamic water supply system. Three pressure measurement points are arranged at 15 cm intervals upstream and downstream of the injection port, which has a diameter of 1 cm and is located at the central segment of the chamber.

The monitoring system comprises a static data acquisition unit (DH3816N), pressure sensors, and a CCD camera, as illustrated in Fig. 8. The data acquisition unit continuously records real-time

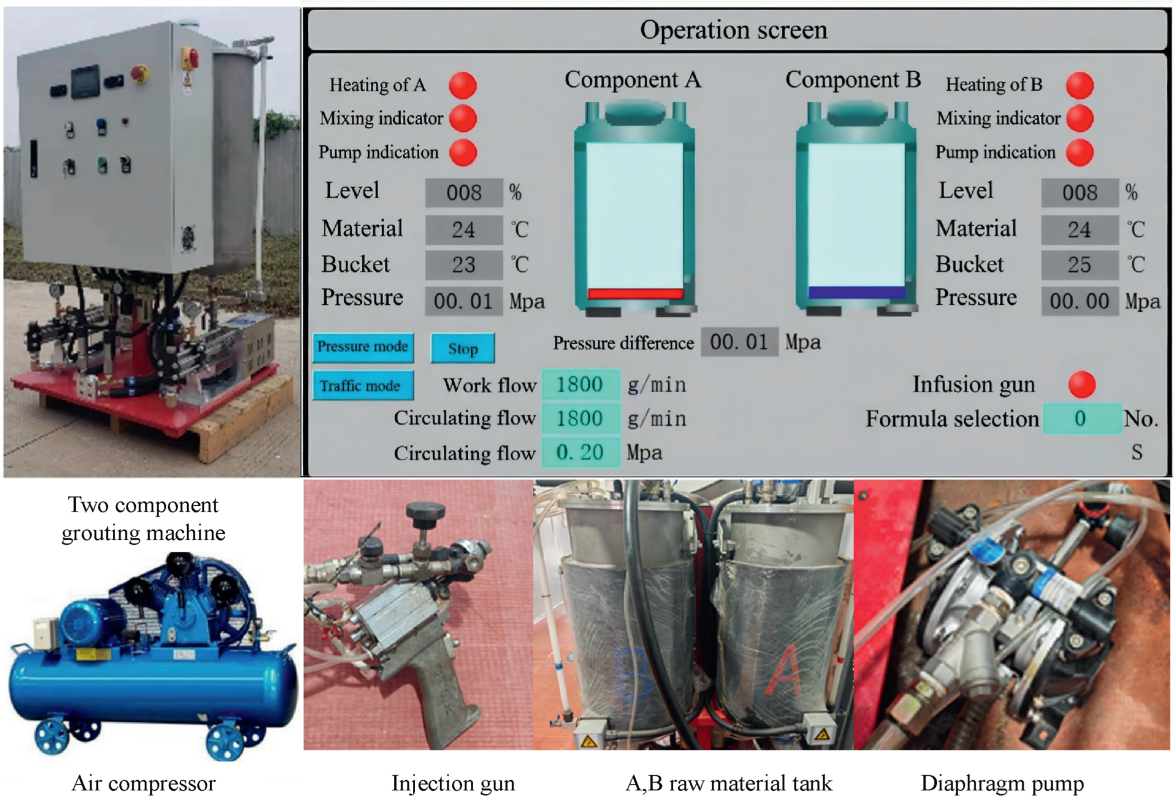

Fig. 6. Dual-component grouting system.

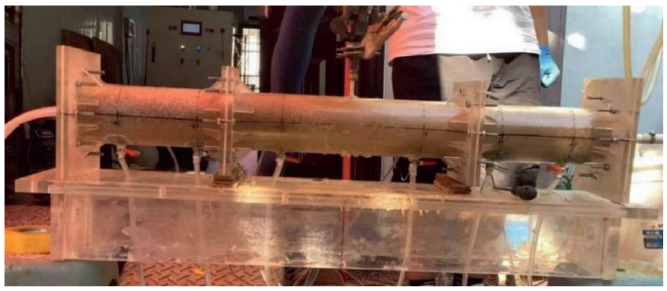

Fig. 7. Visualized diffusion system.

pressure data at multiple locations during the grouting process. It is configured for bridge-type pressure sensors with a bridge resistance of 350 Ω and a sampling frequency of 5 Hz. The pressure sensors have a diameter of 28 mm, a measurement range of 0–0.1 MPa, a resolution of 0.05 kPa, and a sensitivity of 0.00698 mV kPa^{-1}.

The dynamic water supply system consists of a variable-frequency constant-pressure pump, a water tank, and connecting pipelines. Unlike conventional elevated tanks or pressurized air systems, the variable-frequency pump maintains stable water pressure by automatically adjusting the flow rate. When the internal pressure sensor detects an excessive pressure level within the pipeline, the pump reduces the output flow accordingly. Conversely, when the pressure drops below the preset value, the pump increases the discharge flow to restore the target pressure. A large-capacity water tank ensures a continuous and stable water supply, while a filter installed between the tank and the pump prevents impurities from entering the system and clogging the pipelines.

4.3. Experimental procedure

(1) Fix the pressure sensors and miniature valves at the designated monitoring positions. Apply a thin layer of petroleum jelly to the inner wall of the acrylic chamber to prevent adhesion of the polymer slurry, which may affect subsequent tests. Assemble the three acrylic cylindrical segments sequentially using tie rods and bolts, and place silicone gaskets at each interface to ensure airtight sealing. Connect one end of the chamber to the inlet plate with bolts and position the entire device vertically, with the inlet plate resting flat on the ground.

(2) Prepare the granular medium according to the specifications listed in Table 1. Fill the chamber uniformly with the sand material. After filling, assemble the outlet plate and place the chamber in a horizontal position.

(3) Connect the pressure sensors to the data acquisition unit and link the system to the computer via Ethernet. Power on the devices and configure the acquisition parameters through the computer interface.

(4) Connect the dynamic water system to the inlet of the diffusion chamber using flexible hoses. Position the CCD camera in front of the chamber and begin recording to capture the spatial and temporal evolution of slurry diffusion.

(5) Activate the grouting machine and initiate preheating. On the control panel, configure the grouting parameters, including injection pressure, grouting duration, mixing ratio, and preheating temperature for Components A and B. Maintain both components at 40 °C. Secure the grouting gun to the diffusion chamber via the injection pipe, ensuring a tight seal with silicone adhesive. Insert the pipe approximately 5 cm into the chamber.

(6) Briefly open the valve on the dynamic water pump to purge air from the system, then close it. Set the target water pressure and open the inlet valve of the diffusion chamber to initiate steady flow. Zero the pressure sensors and start data recording.

(7) Once steady-state flow is achieved at all monitoring points, begin grouting. If excessive injection resistance occurs, suspend grouting immediately. After complete curing of the

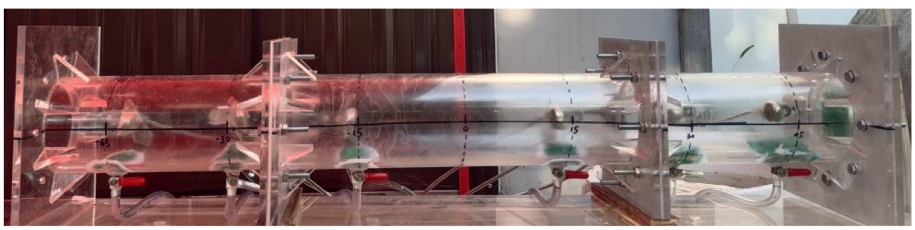

(a) Layout of the monitoring system.

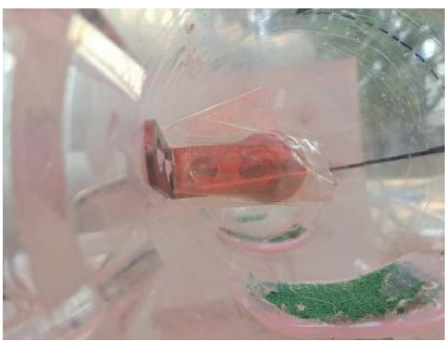

(b) Detailed view of the pressure sensor.

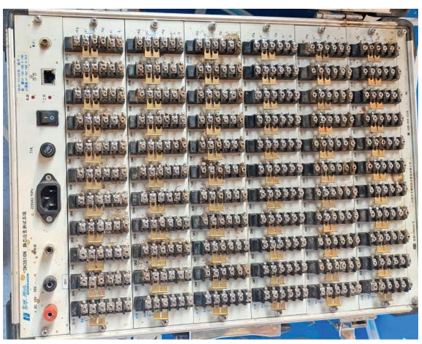

(c) DH3816N-60 static data acquisition instrument.

Fig. 8. Monitoring system.

Table 3
Operating parameters for the model and experimental conditions.

Parameter category	Parameter name	Numerical value
Grouting parameters	Grouting pressure p_0 (pa)	23750
	Grouting time t_m (s)	100
Model parameters	Capillary radius r_0 (m)	0.04
	Grouting hole radius l_0 (m)	0.005
Hydrodynamic parameters	Upstream static water pressure p_{m1} (Pa)	14715
	Downstream static water pressure p_{m2} (Pa)	0
	Water flow velocity v (m/s)	0.1
Porous media parameters	Porosity φ of sand sample 1	30.7 %
	Porosity φ of sand sample 2	37.0 %
	Porosity φ of sand sample 3	42.4 %

slurry, save the recorded pressure–time data and power off the computer, data acquisition unit, and camera. Disassemble the apparatus and measure the effective consolidation length of the sand column in both the upstream and downstream directions.

4.4. Analysis of model validation results

To validate the accuracy of the proposed mathematical model, a comparative analysis was performed between the theoretical predictions and the experimental results under identical boundary and initial conditions. The model parameters were assigned based on the experimental configuration, as summarized in Table 3.

The grout diffusion process under constant-pressure grouting at different time intervals is illustrated in Fig. 9. A high-speed camera continuously recorded the entire process, and digital image processing based on threshold segmentation of red, green, and blue (RGB) values was applied to objectively identify the grout front, thereby minimizing operator subjectivity. During the initial stage (grouting time: 0–20 s; Fig. 9a and b), the polymer grout appeared as a translucent light-yellow fluid with low viscosity and incomplete reaction, diffusing simultaneously in both upstream and downstream directions as the pore water was displaced. As the injection continued (Fig. 9c), the grout concentration and viscosity increased, resulting in a clearer color contrast; the downstream diffusion distance slightly exceeded that upstream. In the later stage (Fig. 9d), the grout had fully reacted, exhibiting a distinct light-yellow central zone surrounded by paler edges. These observations confirm bidirectional diffusion behavior, with the extent and intensity of diffusion evolving progressively as the polymerization reaction proceeded.

Scanning electron microscopy (SEM) images of the solidified polymer–sand composite are presented in Fig. 10. As shown in Fig. 10a–d, the slurry is initially dispersed by numerous water molecules, accompanied by the release of heat and gas within the porous medium. During polymerization, dense micro-pores are generated, indicating preferential reaction of the polymer with water rather than full adhesion to sand particles. In contrast, the microstructures in Fig. 10e and f reveal that, after completion of polymerization, the polymer forms strong interfacial bonding with the sand grains, and the pore spaces are almost completely filled. The resulting microstructure resembles that of a dense soil matrix. The SEM observations further demonstrate that the permeable polymer infiltrates the sand skeleton and reacts to form a cohesive binder. This binder undergoes mild foaming during its interaction with water, enabling it to effectively fill inter-particle voids. After solidification, the material attains considerable strength and impermeability, thereby improving the microstructural compactness of the sand layer and significantly enhancing its mechanical strength and anti-seepage performance.

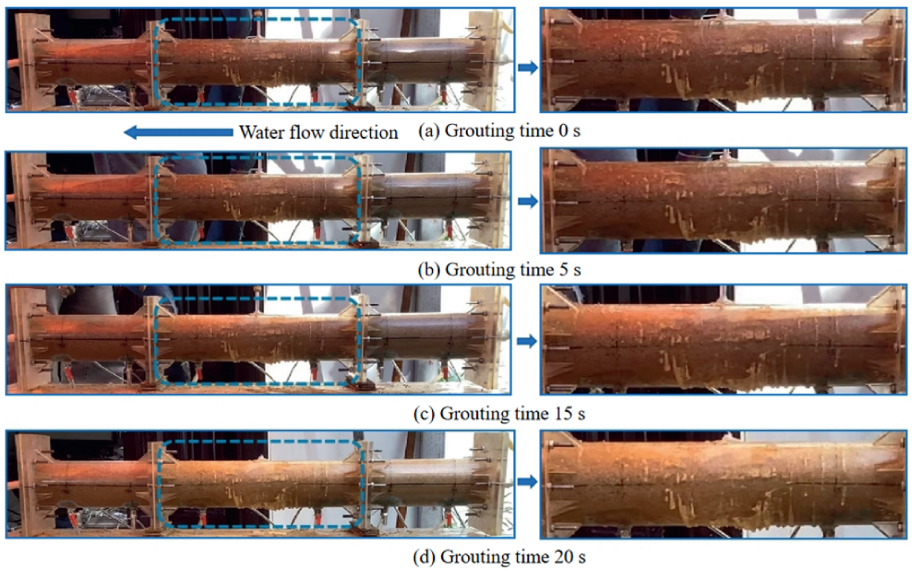

Fig. 9. Grout diffusion images at different time intervals under constant pressure grouting.

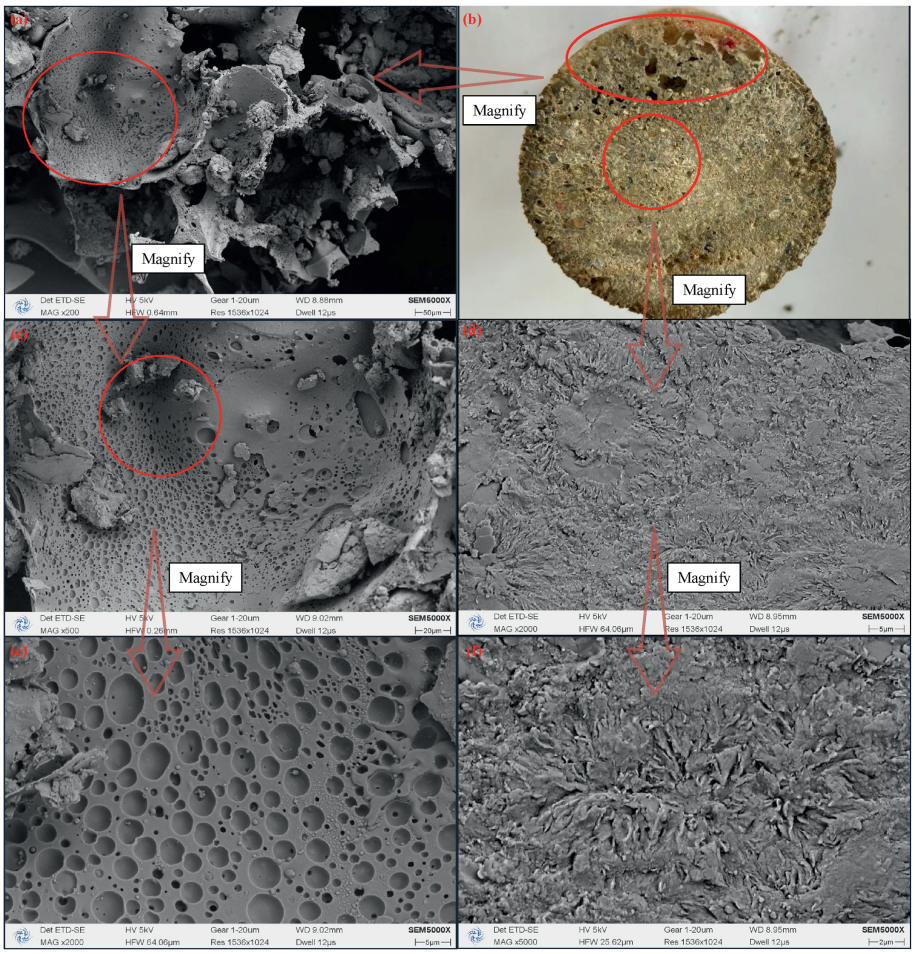

Fig. 10. Comparison of local magnifications of the same sample: (a) 200 × magnification, (b) Consolidation specimen, (c) 500 × magnification, (d) 2000 × magnification, (e) 2000 × magnification, and (f) 5000 × magnification.

Figs. 11–13 illustrate the spatial distribution of slurry pressure obtained from both theoretical modeling and physical experiments. The pressure variation with distance for Sand Sample 1 ($\varphi = 30.7$ %) is shown in Fig. 11. The maximum pressure occurs at the grouting point (0 m) owing to direct injection. With increasing distance, hydraulic resistance accumulates, causing the pressure to decrease and eventually stabilize at larger distances. Co-directional (with-flow) diffusion exhibits lower pressure and a longer diffusion range, whereas counter-directional (against-flow) diffusion shows higher resistance, resulting in elevated pressure and a shorter diffusion distance. The consistency between the experimental and theoretical trends confirms the promoting effect of water flow on slurry transport in porous media.

The pressure variation for Sand Sample 2 ($\varphi = 37$ %) is presented in Fig. 12. The higher porosity reduces flow resistance and facilitates smoother slurry migration. Accordingly, the pressure decreases more gradually with distance, particularly under co-directional flow, leading to a wider diffusion range. These results indicate that increasing porosity enhances slurry mobility by mitigating flow resistance. The results for Sand Sample 3 ($\varphi = 42.4$ %) are shown in Fig. 13. With the highest permeability, the slurry experiences minimal resistance, producing the smoothest pressure gradient and the greatest diffusion range—approximately 0.72 m for co-flow and 0.45 m for counter-flow. These findings consistently demonstrate that greater porosity significantly promotes slurry diffusion, especially in the direction of water flow, whereas counter-flow diffusion remains restricted by elevated hydraulic resistance.

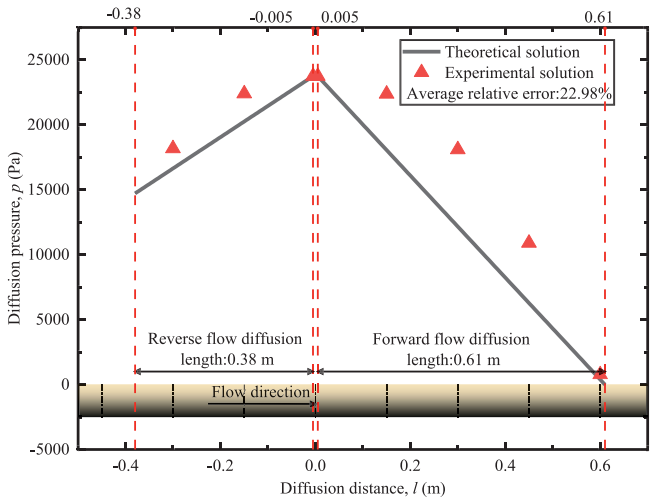

Fig. 11. Variation curve of slurry diffusion pressure with distance (sand sample 1).

Overall, Figs. 11–13 clearly highlight the influence of sand porosity on grout diffusion behavior. As porosity increases, grout diffusion pressure decreases, and diffusion distance increases.

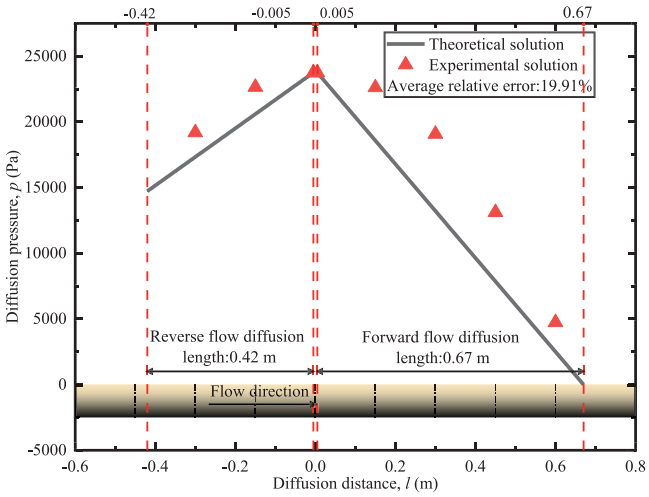

Fig. 12. Variation curve of the slurry diffusion pressure with distance (sand sample 2).

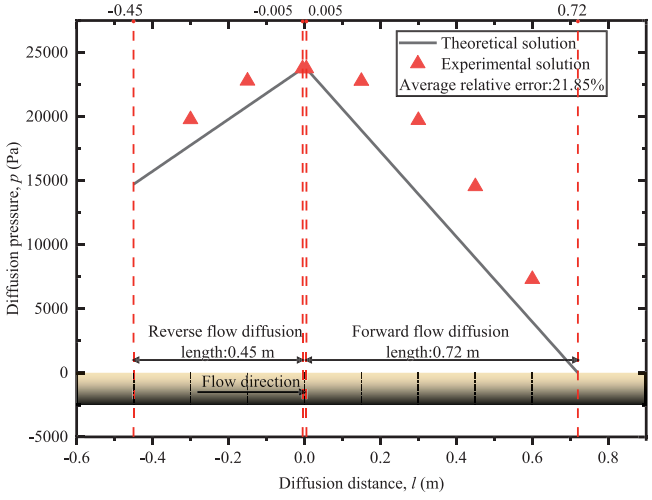

Fig. 13. Variation curve of the slurry diffusion pressure with distance (sand sample 3).

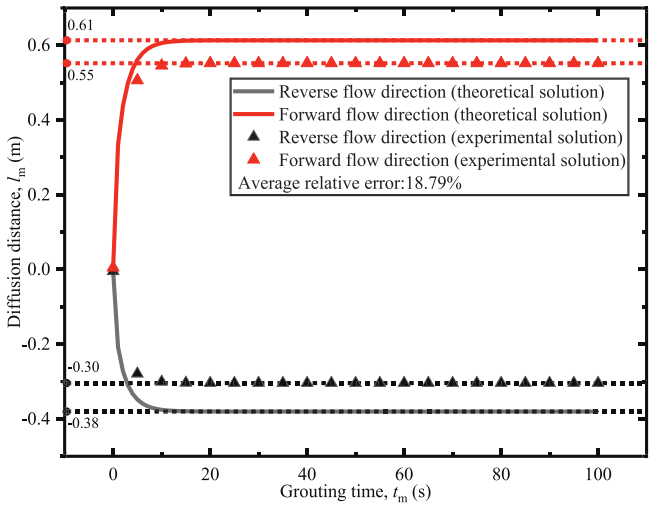

Fig. 14. Variation curves of the grout diffusion distance with respect to the grouting time (sand sample 1).

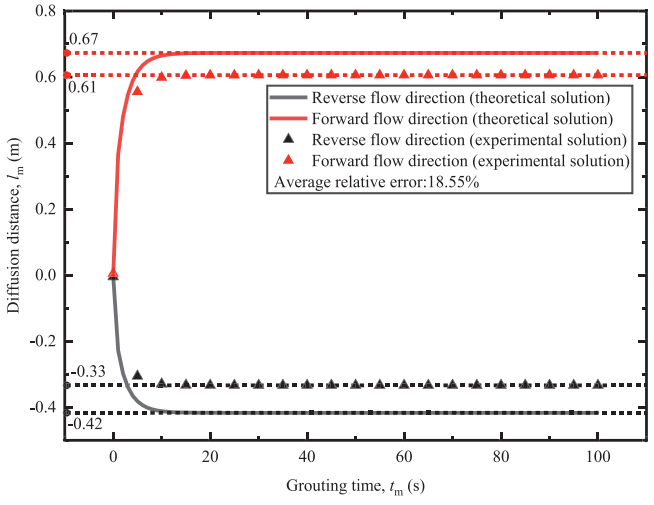

Fig. 15. Variation curve of grout diffusion distance with respect to grouting time (sand sample 2).

Downstream diffusion consistently extends farther than upstream diffusion. The close agreement between the theoretical model and the experimental results confirms that the proposed model accurately predicts the pressure distribution and diffusion characteristics of polymer grout in sand layers with varying porosity under both co-directional and counter-directional flow conditions.

The relationships between slurry diffusion distance and time for different porosities (30.7 %, 37 %, and 42.4 %) are presented in Figs. 14–16. The diffusion behavior in Sand Sample 1 ($\varphi = 30.7$ %) is shown in Fig. 14. During the initial stage (grouting time: 0–20 s), the slurry diffuses rapidly owing to the injection pressure and pore connectivity. As polymerization proceeds and viscosity increases, the slurry fluidity decreases, leading to a gradual reduction in diffusion rate. After approximately 20 s, the diffusion distance stabilizes, reflecting the dominant influence of viscosity. Throughout the process, the co-directional diffusion distance remains greater than the counter-directional distance because counter-flow diffusion encounters higher hydraulic resistance from the opposing water flow.

The diffusion behavior for Sand Sample 2 ($\varphi = 37$ %) is shown in Fig. 15. The higher porosity promotes faster initial diffusion with lower resistance. As solidification advances and viscosity builds up, the diffusion rate decreases and stabilizes after about 20 s. Similar to Sample 1, co-directional diffusion extends farther than counter-directional diffusion owing to reduced resistance along the flow direction. The results for Sand Sample 3 ($\varphi = 42.4$ %) are illustrated in Fig. 16. With the highest porosity, the slurry exhibits the most rapid initial diffusion. However, as polymerization progresses, the increasing viscosity limits further migration, causing the diffusion distance to stabilize at around 20 s. Consistent with the other samples, co-directional diffusion shows a longer range than counter-directional diffusion, which is constrained by greater flow resistance.

Across Figs. 14–16, a consistent trend is evident: grout diffusion proceeds rapidly during the initial stage and gradually slows with time, eventually reaching stabilization. This behavior aligns well with the theoretical model. Higher porosity facilitates faster early-stage diffusion and a greater ultimate diffusion distance, confirming the critical role of pore structure in governing grout migration. In all cases, the downstream diffusion distance exceeds

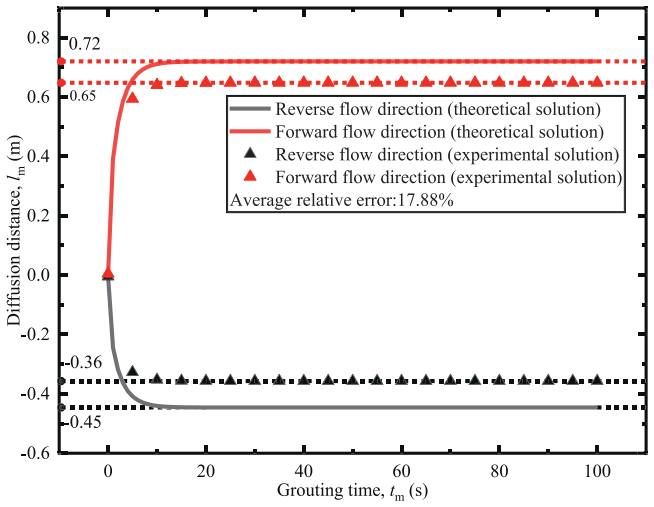

Fig. 16. Variation curves of grout diffusion distance with respect to grouting time (sand sample 3).

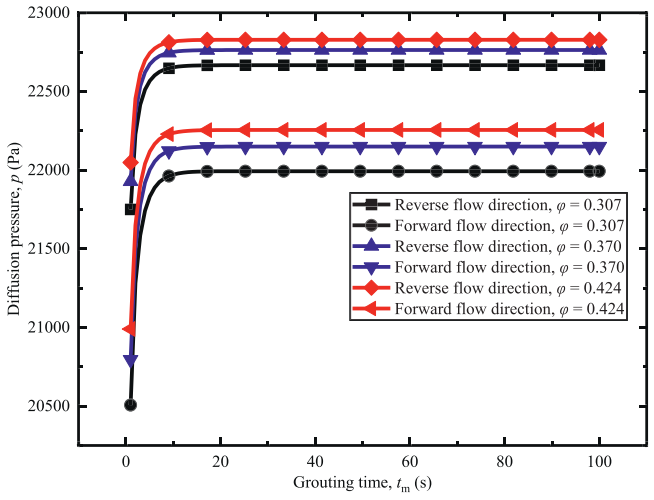

Fig. 17. Variation curves of slurry diffusion pressure with respect to grouting time for different sand layer porosities.

the upstream distance, supporting the theoretical assumption of flow-directional influence. The diffusion curves begin to level off after approximately 20 s, validating the model's prediction that viscosity growth and partial solidification progressively hinder grout movement in the later stages.

The experimental findings substantiate the core assumptions and underlying logic of the proposed theoretical model for grout diffusion in porous media. The staged diffusion characteristics, temporal evolution of diffusion distance, and the effects of porosity and flow direction all show strong qualitative agreement with theoretical predictions. Furthermore, quantitative comparisons reveal that the average relative errors between theoretical and experimental results for both diffusion pressure and diffusion distance are less than 25 %, demonstrating the accuracy and reliability of the model. The results also emphasize that the increase in slurry viscosity caused by polymer solidification markedly restricts diffusion in the later phase of grouting. Overall, the experimental evidence confirms the validity and practical applicability of the proposed mathematical model under dynamic water conditions.

5. Results and discussion

5.1. Analysis of the grout pressure field distribution under different grouting conditions

Figs. 17–21 present the visualized results generated from the theoretical model using the corresponding parameter inputs. These results systematically illustrate the effects of key grouting factors—porosity, hydraulic flow velocity, grouting pressure, and injection location—on the spatial distribution characteristics of the grout pressure field.

The temporal evolution of grout diffusion pressure under both upstream and downstream flow conditions for different sand porosities (φ = 0.307, 0.37, and 0.424) is shown in Fig. 17. Under downstream flow, the grout diffusion pressure increases progressively with time and eventually stabilizes. A similar trend is observed under upstream flow, although the rate of pressure buildup differs. Among the three cases, the sand layer with the highest porosity (φ = 0.424) exhibits the highest peak pressure, while the lowest porosity layer (φ = 0.307) shows the lowest. This indicates that greater porosity provides more pore space for grout propagation, facilitating higher pressure accumulation and more extensive diffusion.

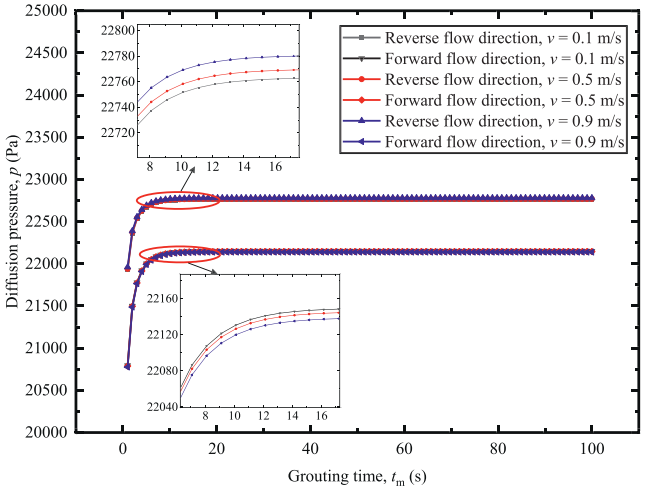

Fig. 18. Variation curve of the slurry diffusion pressure with respect to the grouting time under different hydrodynamic velocities.

The variation in grout diffusion pressure over time at different hydraulic flow velocities (v = 0.1 m/s, 0.5 m/s, and 0.9 m/s) is presented in Fig. 18. In all cases, the grout pressure increases with time and gradually stabilizes. During the early stage, the pressure rises rapidly, but the growth rate decreases as time progresses. Under downstream flow conditions, higher hydraulic velocities (e.g. v = 0.9 m/s) result in lower diffusion pressures and earlier stabilization, indicating that faster flow enhances grout migration and reduces pressure accumulation. In contrast, under upstream flow conditions, higher hydraulic velocities lead to greater diffusion pressure and delayed stabilization, suggesting that resistance increases when the grout moves against the hydraulic gradient, thereby prolonging pressure buildup. For any given flow velocity, the trends differ markedly between upstream and downstream directions: pressure increases more slowly and persists longer in the upstream case, whereas it rises more quickly and stabilizes earlier downstream.

The model-simulated grout pressure distributions under varying grouting conditions—including porosity, hydraulic flow

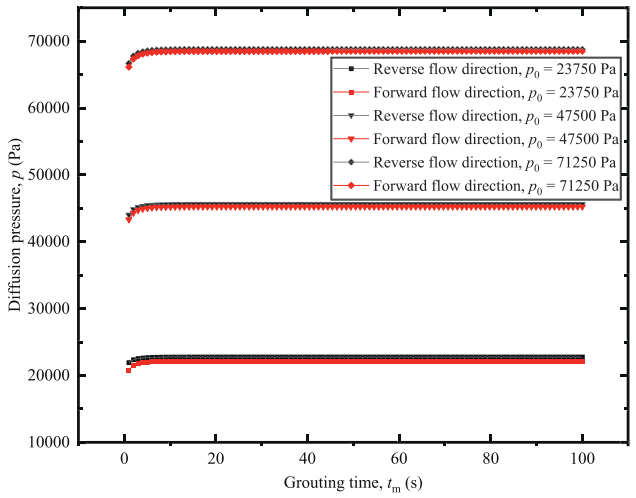

Fig. 19. Variation curves of the slurry diffusion pressure with respect to the grouting time under different grouting pressures.

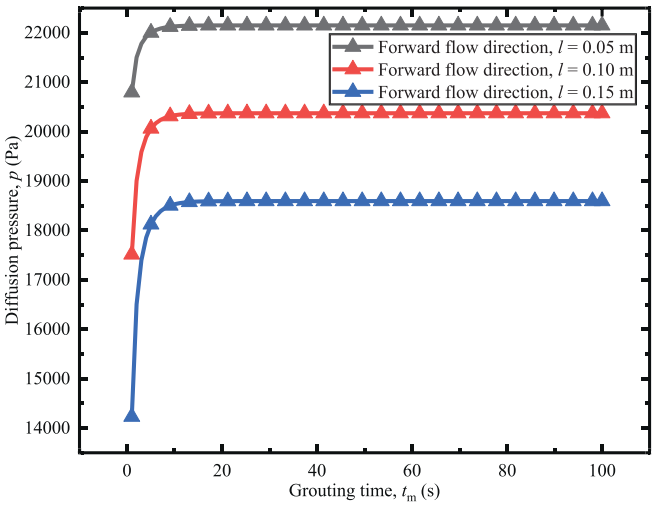

Fig. 21. Variation curves of slurry diffusion pressure with respect to the grouting time at different positions (co-current flow direction).

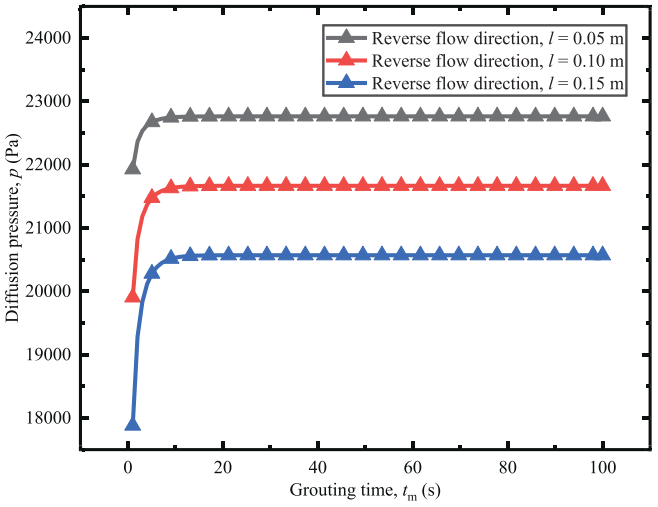

Fig. 20. Curves of the variation in slurry diffusion pressure with respect to the grouting time at different positions (counter-current flow direction).

velocity, grouting pressure, and injection location—are presented in Figs. 17–21. As shown in Fig. 17, a higher porosity (φ = 0.424) produces a greater peak diffusion pressure and faster propagation under both upstream and downstream flows owing to reduced hydraulic resistance. The results in Fig. 18 indicate that, under downstream flow, higher velocities (v = 0.9 m/s) accelerate pressure stabilization and lower the peak pressure, thereby promoting faster grout diffusion. In contrast, under upstream flow, increasing velocity leads to higher pressure and delayed stabilization, reflecting greater hydraulic resistance. Overall, pressure increases more slowly and persists longer in the upstream direction, whereas downstream conditions facilitate faster pressure buildup and earlier stabilization. The effect of the initial grouting pressure (p_0 = 23,750 Pa, 47,500 Pa, and 71,250 Pa) on grout diffusion is shown in Fig. 19. A higher p_0 results in a greater peak pressure and faster stabilization, indicating an enhanced diffusion capacity and improved pressure transmission within the porous medium. Conversely, a lower initial pressure produces limited diffusion and a smaller equilibrium pressure, highlighting the critical role of injection pressure in driving grout penetration and sustaining the overall pressure field.

The variation of slurry diffusion pressure with grouting time at different monitoring positions (l = 0.05 m, 0.1 m, and 0.15 m) in the counter-flow direction is shown in Fig. 20. At l = 0.05 m, the pressure rises rapidly and quickly reaches a relatively high, stable value. In contrast, at l = 0.15 m, the pressure increases more gradually and requires a longer time to stabilize, indicating a slower diffusion rate at greater distances. This behavior demonstrates that in the counter-flow direction, slurry diffusion is impeded by the opposing hydraulic flow, which restricts pressure propagation and causes slurry accumulation near the distal end, thereby forming a higher stable pressure.

The variation curves of the slurry diffusion pressure with respect to the grouting time at different positions (l = 0.05 m, 0.1 m, and 0.15 m) in the direction of flow are shown in Fig. 21. Compared with the counter-flow case, the slurry pressure under co-flow rises more rapidly and stabilizes earlier. This observation indicates that the downstream flow direction facilitates slurry migration, enabling the slurry to be transported and dispersed more effectively by the moving water. Consequently, the peak pressure is lower, and the stabilization occurs earlier, confirming that downstream flow promotes efficient pressure dissipation and diffusion.

The influence of various grouting parameters on the spatial distribution of the slurry pressure field, obtained through theoretical modeling and parameter substitution, is illustrated in Figs. 17–21. Overall, higher porosity corresponds to a more permeable sand layer, leading to a faster increase in diffusion pressure over time and resulting in a higher final stable pressure as well as a broader diffusion range. The hydraulic flow velocity exerts a pronounced directional effect: under co-flow conditions, higher velocities enhance slurry transport but suppress pressure buildup, yielding lower peak pressures; under counter-flow conditions, higher velocities impede slurry migration, causing grout accumulation near the injection point and producing higher stable pressures. Variations in grouting pressure directly influence the driving force of diffusion. Higher initial pressures not only accelerate pressure growth but also sustain elevated diffusion pressures at greater distances from the injection source. Regarding injection location, irrespective of flow direction, the farther the monitoring point is from the injection source, the more delayed the pressure response and the lower the peak pressure. This trend is more

pronounced under co-flow conditions, whereas under counter-flow, cumulative hydraulic resistance can cause the distal pressure to exceed that near the injection point.

5.2. Analysis of slurry flow field characteristics under different grouting parameters

Figs. 22–24 systematically illustrate the effects of key grouting parameters—including porosity, grouting pressure, and water flow direction—on the spatial distribution and temporal evolution of the slurry diffusion field. Fig. 22 presents the variation of slurry interface velocity with grouting time for different sand layer porosities (φ = 0.307, 0.37, and 0.424) under both co-flow and counter-flow conditions. All curves display a general decreasing trend in interface velocity with increasing grouting time, indicating that as grouting progresses, the velocity at the slurry front diminishes and the system gradually approaches a steady state. Initially, the interface velocity is relatively high, reflecting rapid slurry propagation. As diffusion continues, however, the expanding diffusion range, increasing viscosity, and gradual pore filling collectively lead to a rapid decline in velocity. Higher porosity values correspond to higher interface velocities at identical time points, suggesting that greater porosity provides more flow channels and facilitates slurry diffusion. Conversely, lower porosity significantly restricts slurry movement owing to increased hydraulic resistance, resulting in slower diffusion and reduced interface mobility.

The evolution of the slurry interface velocity with time under different hydrodynamic velocities (v = 0.1 m/s, 0.5 m/s, and 0.9 m/s) and flow directions is illustrated in Fig. 23. Under co-flow conditions, a higher water velocity (v = 0.9 m/s) yields a greater slurry interface velocity than lower velocities (e.g. v = 0.1 m/s), indicating that faster ambient flow promotes slurry transport and diffusion. In contrast, under counter-flow conditions, an increase in hydrodynamic velocity results in a reduction in interface velocity. This occurs because slurry diffusion proceeds against the water flow, and stronger opposing hydrodynamic forces hinder slurry advancement, thereby decreasing its overall diffusion rate.

The temporal variations in slurry interface velocity under different initial grouting pressures (p_0 = 23,750 Pa, 47,500 Pa, and 71,250 Pa) are shown in Fig. 24. In all cases, the interface velocity decreases over time, exhibiting a nonlinear attenuation trend. This behavior reflects the combined effects of pore resistance and flow

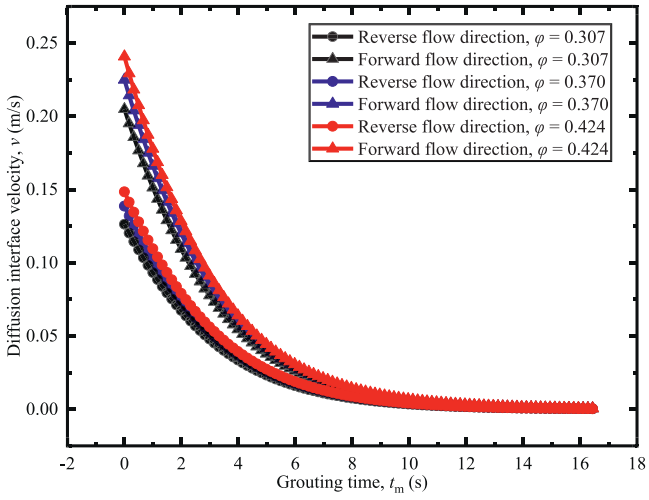

Fig. 22. Variation curves of the grout interface velocity with respect to the grouting time for different sand layer porosities.

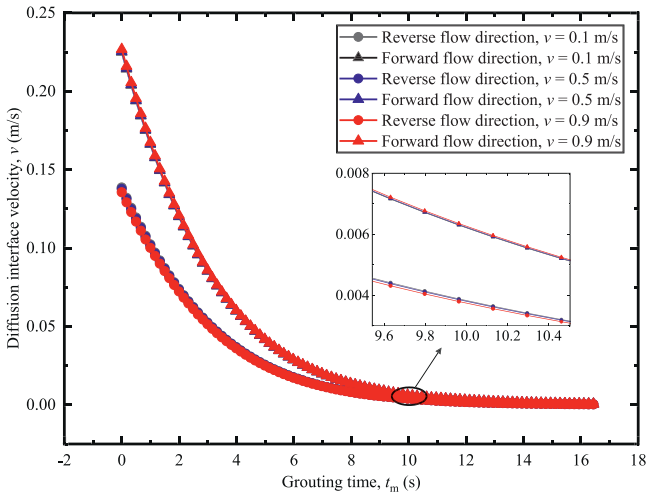

Fig. 23. Variation curves of the grout interface velocity with respect to the grouting time under different hydrodynamic velocities.

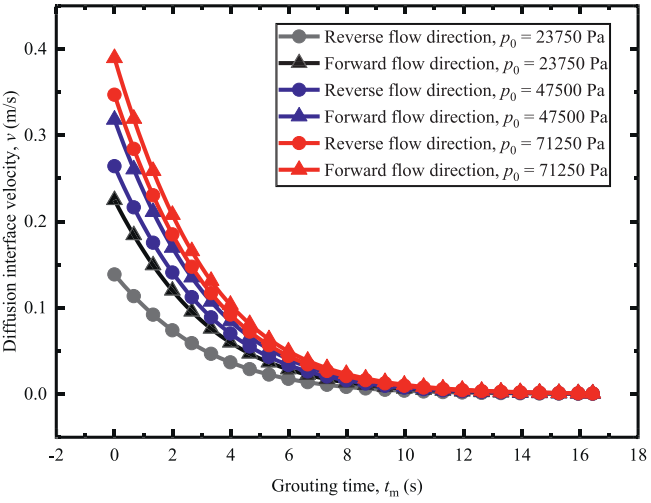

Fig. 24. Variation curves of the grout interface velocity with respect to the grouting time under different grouting pressures.

energy loss during slurry permeation. At the same grouting pressure, the interface velocity under co-flow conditions is markedly greater than that under counter-flow, with the disparity becoming more pronounced as the pressure increases. These results demonstrate that water flow direction can either enhance or suppress slurry diffusion. Moreover, increasing the grouting pressure leads to a higher initial interface velocity and a faster rate of velocity attenuation, confirming that grouting pressure is a critical factor controlling slurry diffusion dynamics.

Porosity, water flow direction, and grouting pressure significantly influence the distribution of the slurry flow field. Increased porosity enhances interface velocity and slurry diffusion, indicating greater permeability and reduced hydraulic resistance. The water flow direction exhibits pronounced anisotropy: diffusion is faster downstream due to synergistic transport, whereas upstream flow impedes diffusion due to opposing forces. Higher grouting pressure accelerates initial diffusion but causes rapid velocity attenuation, suggesting that while it improves diffusivity, it also leads to increased energy dissipation, thus compromising system stability.

5.3. Analysis of slurry diffusion range under different grouting parameters

Figs. 25–27 systematically illustrate the influence of porosity, grouting pressure, and water velocity on the evolution of slurry diffusion distance over time. The influence of sand layer porosity on slurry diffusion distance over time is shown in Fig. 25. This figure presents model-predicted diffusion distances versus time for porosities (φ = 0.307, 0.37, and 0.424), with a rapid initial increase followed by stabilization, indicating nonlinear growth. Higher porosity reduces flow resistance by increasing the number of permeable pathways, thereby enhancing slurry migration according to Darcy's law-based permeability. Key trends include greater diffusion distances at higher porosities, with downstream propagation surpassing upstream due to synergistic water flow, while upstream diffusion is restricted by opposing hydraulic resistance.

The effects of grouting pressure on slurry diffusion characteristics are shown in Fig. 26. The curves depict model-predicted diffusion distances over time under initial grouting pressures (p_0 = 23,750 Pa, 47,500 Pa, and 71,250 Pa). The physical significance lies in the pressure gradient, which drives slurry penetration by overcoming capillary and viscous resistances, modeled via Hagen–Poiseuille principles. Key trends indicate an increase in diffusion distance and growth rate with rising pressure, with the highest pressure case (p_0 = 71,250 Pa) exhibiting the greatest propagation. Downstream diffusion exceeds upstream diffusion due to water flushing, while upstream diffusion is constrained by counter-flow resistance.

The impact of water velocity on slurry diffusion behavior is shown in Fig. 27. This figure illustrates model-predicted diffusion distances versus time for water velocities (v = 0.1 m/s, 0.5 m/s, and 0.9 m/s). Higher velocities introduce shear forces that enhance downstream convection but hinder upstream migration due to counter-flow resistance, as reflected in the model's kinetic analysis. Key trends reveal nonlinear behavior, with rapid early growth followed by stabilization. Downstream diffusion peaks at v = 0.9 m/s, whereas upstream diffusion is severely restricted, with the shortest distance occurring at v = 0.9 m/s.

Overall, slurry diffusion distance increases nonlinearly with grouting time, characterized by rapid initial growth followed by stabilization. Higher porosity enhances slurry migration in porous media, resulting in greater diffusion distances. Increased grouting pressure significantly improves diffusion capacity, with higher pressures yielding more pronounced effects. Under dynamic water conditions, both flow direction and velocity exert complex influences: downstream diffusion consistently exceeds upstream diffusion, with the greatest disparity observed at a flow velocity of 0.9 m/s. In contrast, higher flow velocities in the upstream direction suppress slurry diffusion, indicating strong hydrodynamic inhibition.

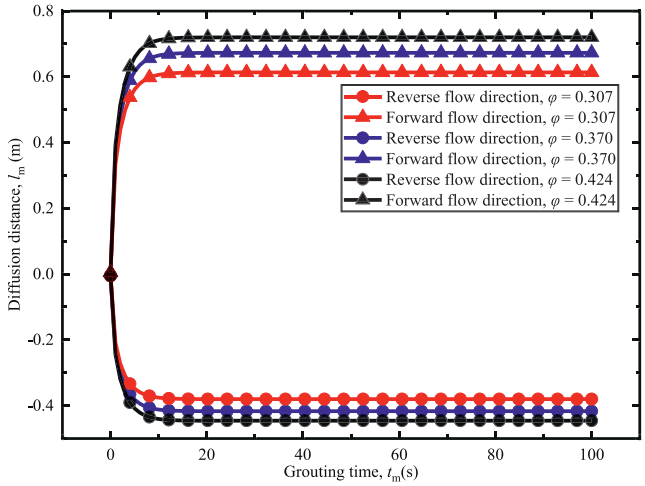

Fig. 25. Variation curves of the slurry diffusion distance with respect to the grouting time for different sand layer porosities.

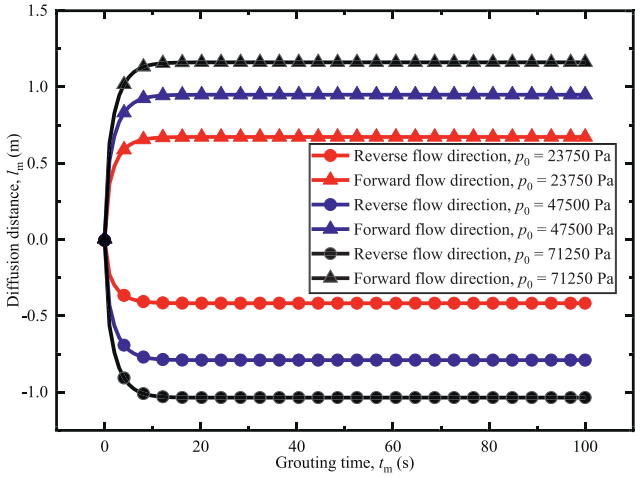

Fig. 26. Variation curves of grout diffusion distance with respect to grouting time under different grouting pressures.

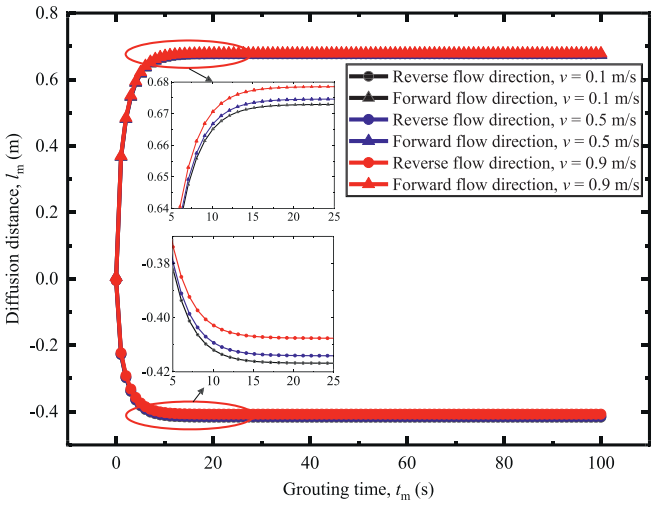

Fig. 27. Variation curves of slurry diffusion distance with respect to grouting time under different hydrodynamic velocities.

5.4. Comparative analysis of real-time slurry diffusion characteristics in pore and void media

To investigate the differences in slurry diffusion between porous and void media, a comparative analysis was conducted focusing on pressure distribution, diffusion distance evolution, and interface velocity. In this study, porous media are defined as granular materials with relatively small pore throats (typically less than 2–3 times the mean particle diameter, d_{50}), where fluid

migration occurs mainly through interconnected fine pores, following Darcy-type seepage behavior. In contrast, void media are defined as materials containing large, continuous, and highly connected cavity structures (with pore openings much greater than 3–5 times d_{50}), in which slurry migration is primarily governed by cavity filling processes rather than pore-scale seepage.

Fig. 28 shows the variation of slurry pressure with diffusion distance under both media types and flow directions. In all cases, slurry pressure decreases monotonically along the diffusion path, indicating pressure loss with increasing distance. Compared to porous media, void media exhibit slower pressure attenuation and maintain higher pressures over a longer range, suggesting that the dense structure of porous media imposes greater resistance to slurry migration. Additionally, slurry pressure is consistently lower in the downstream direction than upstream, implying that downstream flow facilitates slurry propagation with lower pressure gradients, while upstream flow increases hydraulic resistance, resulting in faster pressure decay and higher pressure levels.

Fig. 29 presents the evolution of slurry diffusion distance over time in both void and porous media under downstream and upstream flow conditions. Regardless of media type or flow direction, diffusion distance increases nonlinearly with grouting time. In void media, diffusion progresses rapidly, with significantly greater distances in the downstream direction, highlighting the strong influence of flow direction on slurry migration. In contrast, porous media exhibit reduced diffusion distances and smaller differences between flow directions, suggesting that the porous structure diminishes the effect of flow orientation.

Fig. 30 compares the evolution of interface velocity under different conditions. In all cases, interface velocity decreases over time, reflecting the gradual stabilization of the diffusion process. Void media, with continuous cavities and minimal resistance, allow faster slurry propagation, resulting in higher interface velocities compared to porous media, where dense microstructures restrict flow. In void media, downstream flow notably enhances interface velocity due to hydrodynamic assistance, while upstream flow suppresses slurry advancement. However, in porous media, structural resistance dominates, diminishing the impact of flow direction and reducing velocity differences between downstream and upstream conditions.

In summary, slurry diffusion behavior differs significantly between porous and void media. In both media, pressure decreases monotonically with diffusion distance. However, void media exhibit slower pressure attenuation due to their continuous cavity structure, while porous media show rapid pressure loss owing to disconnected or tortuous pore channels. Regarding diffusion distance, slurry propagates more efficiently in void media, with a pronounced difference between downstream and upstream directions, indicating a strong flow-induced enhancement. In porous media, high structural resistance limits diffusion, even under favorable flow conditions. For interface velocity, void media allow rapid initial slurry advancement with significant directional differences, whereas in porous media, structural resistance dominates, reducing the impact of flow direction.

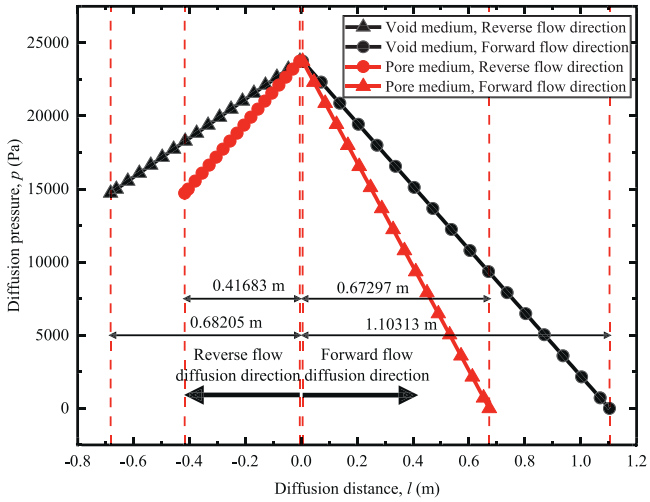

Fig. 28. Variation curves of slurry diffusion pressure with distance (void medium and porous medium).

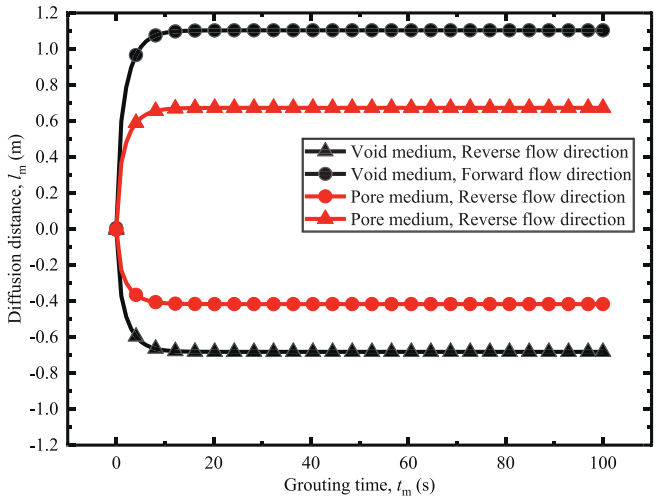

Fig. 29. Variation curves of grout diffusion distance with grouting time (void medium and porous medium).

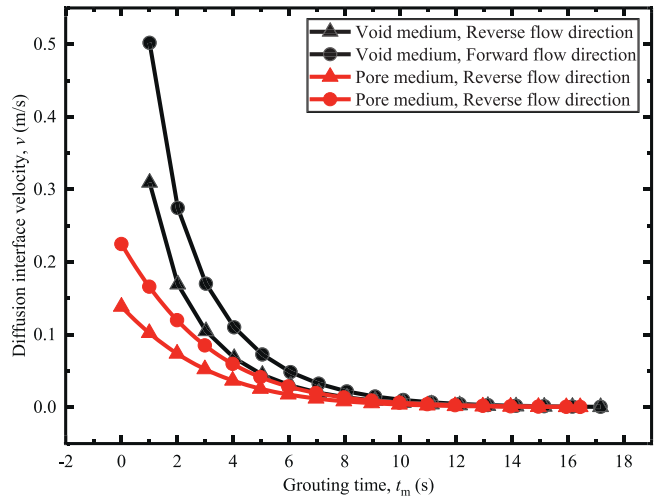

Fig. 30. Variation curves of grout interface velocity with grouting time (void medium and porous medium).

6. Conclusions

This study explores the diffusion mechanism of polymer slurry in water-rich sandy soils during permeation grouting, integrating theoretical modeling and experimental validation to clarify slurry behavior under complex geological conditions and inform geotechnical engineering practices. Based on Darcy's law, Hagen–Poiseuille flow theory, and Newtonian fluid assumptions, a

diffusion model was developed, accounting for the effects of porous sand and water flow on pressure, flow fields, and diffusion range. Constant-pressure grouting tests using a custom-developed visual simulation system validated the model, analyzing factors such as media type, grouting pressure, flow direction, and velocity. The main conclusions are as follows:

(1) Constant-pressure dynamic water grouting tests were conducted using a custom-developed visual simulation system. The experimental results showed a high degree of consistency with the theoretical predictions, validating the model's accuracy and reliability. Observations revealed that slurry diffusion distance and velocity were significantly greater in the co-flow direction than in the counter-flow direction, confirming the model's assumptions regarding flow-assisted diffusion. Additionally, the diffusion process exhibited staged characteristics: rapid expansion in the early phase, followed by a gradual decrease due to increased viscosity and gelation, and ultimately stabilizing. These findings further affirm the effectiveness of the model in describing the dynamic behavior of slurry diffusion.

(2) This study systematically investigates the effects of grouting pressure, porosity, and water flow velocity on slurry diffusion behavior. Grouting pressure, as the primary driving force, significantly influences the pressure field, flow dynamics, and diffusion extent. Higher grouting pressures overcome medium resistance, leading to enhanced penetration depth and broader diffusion. The experimental results revealed that under high-pressure conditions, the pressure distribution is more uniform and decays more slowly, indicating more effective slurry propagation.

(3) The porosity of the sand layer governs the resistance distribution and flow paths. In high-porosity media ($\varphi = 42.4$ %), the slurry exhibits higher flow velocity and a wider diffusion range (0.72 m) with more uniform flow fields. In contrast, low-porosity media ($\varphi = 30.7$ %) restrict diffusion (0.45 m) and result in uneven flow patterns. Additionally, water flow direction exerts a significant influence on slurry migration. Co-directional flow enhances slurry velocity and diffusion through a synergistic effect, whereas counter-directional flow increases resistance and inhibits diffusion. These effects are further amplified at higher water velocities ($v = 0.9$ m/s), particularly under co-flow conditions.

(4) This study compared slurry diffusion in porous sand and void media, revealing the critical role of the medium structure. In porous media, the slurry encounters high resistance, causing rapid pressure decay, limited diffusion (max 0.72 m), and slow, uniform interface movement. In void media, slurry spreads freely with minimal resistance, resulting in broader diffusion, slower pressure decay, and a higher initial interface velocity (0.12 m/s), albeit with uneven surges. Water flow direction has a limited effect on slurry diffusion in porous media due to pore constraints, but significantly influences void media, enhancing co-flow and suppressing counter-flow dispersion. Thus, grouting in porous media requires uniform coverage, while void media grouting results in rapid, unstable diffusion.

CRediT authorship contribution statement

Jiasen Liang: Writing – original draft, Investigation. **Xueming Du:** Conceptualization, Formal analysis. **Lei Wang:** Writing – review & editing. **Hongyuan Fang:** Investigation, Supervision. **Xiaohua Zhao:** Supervision, Validation, Writing – review & editing. **Bin Li:** Validation, Writing – review & editing. **Kejie Zhai:** Supervision, Writing – review & editing. **Shanyong Wang:** Project administration, Resources.

Declaration of competing interest

The authors declare that they have no known competing financial interests or personal relationships that could have appeared to influence the work reported in this paper.

Acknowledgments

This work was supported by the National Natural Science Foundation of China (Grant No. 52578491), the Outstanding Youth Fund for Natural Science of Henan Province (Grant No. 232300421064), and the Program for Science and Technology Innovation Talents in Universities of Henan Province (Grant No. 25HASTIT014).

List of symbols

A, B, C	Viscosity parameters
c_1, c_2, c_3, c_4	Constant of integration
C_u	Uniformity coefficient
C_c	Coefficient of curvature
d_{60}	Particle diameter at a cumulative throughput of 60%
d_{30}	Particle diameter at a cumulative throughput of 30%
d_{10}	Particle diameter at a cumulative throughput of 10%
k	Permeability coefficient
p_w	Radial water pressure (Pa)
l	Radial distance at any position (m)
l_m	Effective diffusion distance (m)
l_0	Radius of the grouting borehole (m)
p_m	Hydrostatic pressure (Pa)
p_0	Injection (grouting) pressure (Pa)
p	Radial diffusion pressure of slurry (Pa)
$\frac{dp}{dl}$	Pressure gradient in the radial direction
q	constant grouting flow rate (m^3/s)
r_0	Radius of the idealized cylindrical pore or capillary (m)
r	Radial radius at any position (m)
S	Cross-sectional area of the flow channel (m^2)
t_m	Total grouting time (s)
u_{pore}	Actual average velocity within the pores (m/s)
$\overline{u_l}$	Average flow velocity of slurry (m/s)
u_l	Slurry flow rate (m/s)
$\frac{du_l}{dr}$	velocity gradient representing the rate of change of slurry velocity in the radial direction
V	Seepage velocity (m/s)
v	Velocity of water flow (m/s)
ρ_w	Density of water (kg/m^3)
τ	Shear stress exerted on the slurry during flow (Pa)
$\eta_{(t)}$	Time-dependent viscosity of the slurry (mPa s)
φ	Porosity of porous media (%)

References

Baser, S.A., Khakhar, D.V., 1994. Modeling of the dynamics of R-11 blown polyurethane foam formation. Polym. Eng. Sci. 34, 632–641.

Budd, P.M., McKeown, N.B., 2010. Highly permeable polymers for gas separation membranes. Polym. Chem. 1, 63–68.

Cambefort, H., 1977. The principles and applications of grouting. Q. J. Eng. Geol. Hydrogeol. 10, 57–95.

Castro, J.M., Macosko, C.W., 1980. Kinetics and rheology of typical polyurethane reaction injection molding systems. In: Proceedings of Soc Plast Eng Tech Pap Annu Tech Conf, 38th, Plast Prog Through Process, pp. 434–438. New York, NY, USA.

Dagan, G., 1979. The generalization of Darcy's law for nonuniform flows. Water Resour. Res. 15, 1–7.
Du, X., Liu, C., Wang, C., Fang, H., Xue, B., Gao, X., Han, Y., 2022. Diffusion characteristics and reinforcement effect of cement slurry on porous medium under dynamic water condition considering infiltration. Tunn. Undergr. Space Technol. 130, 104766.
Du, X.M., Liu, C., Meng, X.X., Rui, Y.C., Fang, H.Y., Li, B., Zhai, K.J., Zhang, C., Du, M.R., Xue, B.H., 2025. Diffusion law of nonaqueous reactive expansive polymers in sand and gravel media. J. Cent. South Univ. 32, 420–436.
Hao, Y., Guo, C., Shi, M., Wang, F., Xia, Y., Wang, C., 2023. Application of polymer split grouting technology in earthen dam: diffusion law and applicability. Constr. Build. Mater. 369, 130612.
Ke, Q., Guo, C., Wang, F., Chu, X., Zhai, K., 2024. Investigations on the seepage characteristics of polymer grouting body for repairing HDPE geomembrane defects based on LF NMR. Constr. Build. Mater. 414, 135004.
Letourneur, J., 1991. Grouting theory and practice, 1989. In: Nonveiller, E. (Ed.), Eng. Geol., 31. Elsevier, Amsterdam, p. 250 (3–4), 374.
Li, S., Ma, C., Liu, R., Chen, M., Yan, J., Wang, Z., Duan, S., Zhang, H., 2021. Super-absorbent swellable polymer as grouting material for treatment of karst water inrush. Int. J. Min. Sci. Technol. 31, 753–763.
Li, P., Liu, J., Shi, L., Li, X., Zhu, H., Huang, D., Kou, X., 2022. Two-phase analytical model of seepage during grout consolidation around shield tunnel considering the temporal variation in viscosity and the infiltration effect. Eur. J. Environ. Civ. Eng. 26, 4392–4415.
Li, Z., Zhu, Z., Zhao, Y., Zeng, C., Zhang, P., 2022. Experimental investigation on the diffusion law of polymer slurry grouted in sand. Polymers 14, 3635.
Liang, J., Du, X., Fang, H., Du, M., Shi, M., Gao, X., Han, Y., 2022. Numerical and experimental study of diffusion law of foamed polymer grout in fracture considering viscosity variation of slurry. Tunn. Undergr. Space Technol. 128, 104674.
Liang, J., Du, X., Fang, H., Li, B., Wang, N., Di, D., Xue, B., Zhai, K., Wang, S., 2024. Intelligent prediction model of a polymer fracture grouting effect based on a genetic algorithm-optimized back propagation neural network. Tunn. Undergr. Space Technol. 148, 105781.
Liang, J., Du, X., Fang, H., Zhao, X., Li, B., Zhai, K., Sun, M., Wang, S., 2025. Optimal formulation design of silicate-modified polymer based grouting material for reinforcing silty fine sand stratum. Polym. Test. 149, 108840.
Liu, B., Jiang, X., Meng, S.Y., Yang, Y., 2025. Study on slope deformation mechanism under combined infiltration of rainfall and water. Water Res. Hydropower Eng. 56, 202–211.
Long, Y., Tan, Y., 2020. Soil arching due to leaking of tunnel buried in water-rich sand. Tunn. Undergr. Space Technol. 95, 103158.
Ma, L., Chen, S., Tian, L., Yu, H., Wu, P., 2025. Study on the water pathway exploration and the geological model construction of the mine in karst area. Water Res. Hydropower Eng. 56, 203–216.
Markou, I.N., Christodoulou, D.N., Petala, E.S., Atmatzidis, D.K., 2018. Injectability of microfine cement grouts into limestone sands with different gradations: experimental investigation and prediction. Geotech. Geol. Eng. 36, 959–981.
Peng, S., Luo, J., Luo, G., Pan, H., Cao, H., 2024. Laboratory modelling on sand erosion caused by tunnel leakage in water-rich sandy strata. Acta Geotech. 19, 8089–8110.
Seo, D., Youn, J.R., 2005. Numerical analysis on reaction injection molding of polyurethane foam by using a finite volume method. Polymer 46, 6482–6493.
Sharghi, M., Chakeri, H., Ozcelik, Y., 2017. Investigation into the effects of two component grout properties on surface settlements. Tunn. Undergr. Space Technol. 63, 205–216.
Sun, X., Wang, Y., Liu, H., Yang, Z., Ma, H., 2024. Development of multivariate-coupled grouting diffusion model for RCC. Constr. Build. Mater. 435, 136748.
Wang, Y., Xie, C., 2022. Uniform structural stability of Hagen–Poiseuille flows in a pipe. Commun. Math. Phys. 393, 1347–1410.
Wang, Y., Han, M., Li, B., Wan, Y., 2022. Stability evaluation of earth-rock dam reinforcement with new permeable polymer based on reliability method. Constr. Build. Mater. 320, 126294.
Wang, H., Yu, Y., Zhang, P., Yang, C., Wen, H., Zhang, F., Du, S., 2024. Study on the diffusion mechanism of infiltration grouting in fault fracture zone considering the time-varying characteristics of slurry viscosity under seawater environment. Int. J. Concr. Struct. Mater. 18, 65.
Xu, C., Jiang, H., Zhang, Y., Wu, X., Gao, P., Sun, D., Wang, H.J., 2024. Study on penetration resistance and infiltration field characteristics of bucket foundation. Water Res. Hydropower Eng. 55, 182–195.
Yang, K., Fang, H., Zhang, X., Du, X., Li, B., Zhai, K., 2024. Mechanical evaluation analysis of pipe-liner composite structure before and after polymer grouting rehabilitation. Eng. Fail. Anal. 158, 108050.
Ye, F., Yang, T., Mao, J., Qin, X., Zhao, R., 2019. Half-spherical surface diffusion model of shield tunnel back-fill grouting based on infiltration effect. Tunn. Undergr. Space Technol. 83, 274–281.
Yuce, M.I., Muratoglu, A., 2015. Hydrokinetic energy conversion systems: a technology status review. Renew. Sus. Energ. Rev. 43, 72–82.
Zhang, X., Wang, E., 2024. Study on the gelation process and mechanical properties of organic polymer grouting materials applied to fissure sealing in underground mines. Polymers 16, 446.
Zhou, Z., Du, X., Wang, S., Cai, X., Chen, L., 2019. Micromechanism of the diffusion of cement-based grouts in porous media under two hydraulic operating conditions: constant flow rate and constant pressure. Acta Geotech. 14, 825–841.
Zhu, Y., Sun, H., Xu, S., Hu, L., Cao, H., Cai, Y., Liu, J., 2023. Mechanics of the penetration and filtration of cement-based grout in porous media: new insights from CFD–DEM simulations. Tunn. Undergr. Space Technol. 133, 104928.
Zhu, G., Guo, S., Shi, J., Zhang, Q., 2025. Study on the diffusion mechanism of columnar-hemispherical infiltration grouting form of quick-setting slurry considering spatial and temporal variations of slurry viscosity. Phys. Fluids 37, 017101.

Xueming Du received his PhD degree from the School of Resources and Safety Engineering at Central South University. He is currently a tenure-track researcher at the School of Water Conservancy and Transportation, Zhengzhou University. His research focuses on the control of adverse geological hazards in underground engineering, the development of novel grouting materials, and intelligent evaluation techniques. He proposed an integrated rapid multi-scale detection technology for urban pavement structures based on coupled dynamic and electromagnetic methods. He established coupled diffusion models for different types of grouts (particle-based and permeable/foaming chemical types) in porous and fractured media, revealing the mechanisms by which grout fluid properties and the characteristics of pore and fracture structures influence grout diffusion behavior. Furthermore, he developed a complete set of precision grouting repair technologies for full-space restoration of urban pavement bases and subgrades.